Rapid Fault Leakage Screening for CO_2 Storage Under Uncertainty: Application to a Faulted Miocene Aquifer in the Malay Basin

Hariharan Ramachandran[1*], Iain de Jonge-Anderson[1,2], Ana Widyanita[3], Uisdean Nicholson[1], Andreas Busch[4,5], Sebastian Geiger[6], Florian Doster[1,5]

[1] Institute of GeoEnergy Engineering, Heriot-Watt University, Edinburgh, UK
[2] Department of Civil & Environmental Engineering, University of Strathclyde, Glasgow, UK
[3] PETRONAS Research Sdn Bhd, Bangi, Malaysia
[4] Lyell Centre, Heriot-Watt University, Edinburgh, UK
[5] Subsurface Energy Transition and Innovation Centre, Heriot-Watt University, Edinburgh, UK
[6] Department of Geoscience and Engineering, Delft University of Technology, Delft, Netherlands

* Correspondence: Hariharan Ramachandran, h.ramachandran@hw.ac.uk
ORCiD: 0000-0001-5979-0930 (HR)

Rapid Fault Leakage Screening for CO_2 Storage Under Uncertainty: Application to a Faulted Miocene Aquifer in the Malay Basin

Hariharan Ramachandran[1*], Iain de Jonge-Anderson[1,2], Ana Widyanita[3], Uisdean Nicholson[1], Andreas Busch[4,5], Sebastian Geiger[6], Florian Doster[1,5]

[1] Institute of GeoEnergy Engineering, Heriot-Watt University, Edinburgh, UK
[2] Department of Civil & Environmental Engineering, University of Strathclyde, Glasgow, UK
[3] PETRONAS Research Sdn Bhd, Bangi, Malaysia
[4] Lyell Centre, Heriot-Watt University, Edinburgh, UK
[5] Subsurface Energy Transition and Innovation Centre, Heriot-Watt University, Edinburgh, UK
[6] Department of Geoscience and Engineering, Delft University of Technology, Delft, Netherlands

* Correspondence: Hariharan Ramachandran, h.ramachandran@hw.ac.uk
ORCiD: 0000-0001-5979-0930 (HR)

Abstract

Geological CO_2 storage is critical for mitigating climate change, yet the risk of leakage along faults poses significant challenges. Faults function as structural traps or preferential CO_2 migration pathways depending on their sealing capacity. This study applies a computationally efficient rapid fault leakage analysis tool that combines a vertically integrated reservoir model with an upscaled fault leakage function based on steady-state flow approximations, conceptualising faults as zones of increased vertical and reduced horizontal permeability. The methodology is applied to faulted Miocene clastic aquifers in the Malay Basin, representing a complex, structurally heterogeneous setting typical of mature Southeast Asian storage prospects. The analysis evaluates 600 well locations to identify optimal injection sites, incorporating both deterministic scenarios (fully sealing versus leaking faults) and comprehensive uncertainty quantification across fault property heterogeneity. Comparison of sealing and leaking scenarios establishes physical controls governing leakage behaviour, while uncertainty quantification using 10,000 Monte Carlo realisations across 71 parameters (fault-specific permeability, capillary entry pressure, and transmissibility for 23 faults, plus reservoir properties) identifies the dominant controls on leakage outcomes. First, leakage sensitivity concentrates on a small fault subset: only 5 of 23 faults exhibit Spearman correlation with outcomes, with a single fault dominating system response. Second, k-medoids clustering identifies three distinct regimes, with high-leakage scenarios comprising 44% of realisations, the modal outcome rather than a rare event under current parameter uncertainty. Third, cluster membership is predominantly controlled by Fault 23 permeability, while Fault 1 transmissibility controls lateral access to the northern fault array, a cascade pathway that demonstrates the value of multi-fault uncertainty quantification. The findings demonstrate that targeted characterisation of 5-

7 critical faults can effectively collapse predictive uncertainty, enabling transition from high-uncertainty screening to confident operational planning. The tool's computational efficiency enables rapid assessment supporting early-stage site screening, risk assessment, and targeted data acquisition, thereby accelerating the identification and prioritisation of secure CO_2 storage sites.

Keywords: CO_2 storage, fault leakage, vertical equilibrium modelling, cluster analysis, faulted aquifers, uncertainty quantification

1 Introduction

Geological CO_2 storage is indispensable for mitigating climate change and achieving global decarbonization targets (Krevor et al. 2023). Malaysia's National Energy Transition Roadmap exemplifies this urgency, targeting CO_2 storage capacities of 15 million tonnes per annum (Mtpa) by 2030 and 80 Mtpa by 2050 (Fernandez et al., 2024). Meeting these targets requires systematic evaluation of storage prospects across diverse geological settings to ensure long-term safe containment within these formations. Leakage compromises mitigation efforts, poses environmental and health risks, and can undermine public confidence (Bielicki et al., 2015; Ashworth et al., 2015; Jones et al., 2017). Regulatory frameworks therefore require comprehensive geological characterisation and rigorous site assessment to identify and mitigate leakage risks (Dixon et al., 2015).

Faults play a critical role in storage viability, functioning either as structural traps that enhance containment or as preferential pathways for upward CO_2 leakage when their sealing capacity is compromised (Caine et al., 1996; Dixon et al., 2015). Fault zone architecture produces a strong permeability contrast between fault zone components: fault cores exhibit permeabilities several orders of magnitude below the surrounding protolith, while fractured damage zones can be 1–3 orders of magnitude more permeable than the host rock, creating preferential pathways for along-fault fluid migration (Bense and Pearson, 2006; Faulkner et al., 2010; Bense et al., 2013; Scibek, 2020). Damage zone width scales with fault displacement, and permeability varies systematically with fracture density and connectivity across the fault zone (Childs et al., 2009; Faulkner et al., 2011). The capillary sealing capacity of fault damage zones is governed by fracture aperture distributions and clay content rather than the intact matrix entry pressures relevant to unfaulted caprocks, with effective values spanning several orders of magnitude depending on fracture fill mineralogy and connectivity (Guiltinan et al., 2018; Phillips et al., 2020).

Hydraulic properties of fault zones are poorly constrained at early screening stages and span multiple orders of magnitude even within the same geological setting (Miocic et al., 2019b; Scibek, 2020). This parameter uncertainty translates directly into outcome uncertainty by substantially altering predicted storage capacity in fault-bounded reservoirs. Recent ensemble-based approaches have addressed fault leakage uncertainty through stochastic upscaling with copula representation (Pettersson et al., 2025), deep-learning surrogates for coupled flow-geomechanics (Lu et al., 2025), and probabilistic transmissibility models (Salo-Salgado et al., 2025), but each of these studies characterises a single fault zone in isolation. In storage settings with many faults, identifying which fault properties drive leakage outcomes, and therefore which

measurements would most efficiently reduce predictive uncertainty, requires systematic ensemble analysis across the full fault population.

Traditional reservoir simulation approaches using fine-scale coupled models are computationally prohibitive for evaluating multiple sites or conducting comprehensive uncertainty quantification with thousands of parameter combinations (Birkholzer et al., 2012; Ringrose & Meckel, 2019). These combined data and computational limitations constrain early-stage decision making. Rapid assessment tools can address these limitations by accelerating CO_2 storage deployment through reduced early-stage project risks and costs while maintaining sufficient accuracy for screening purposes.

In this study, we address this early stage in the exploration funnel and build on the rapid fault leakage framework developed by Ramachandran et al. (2026). Our previous work combines a vertically integrated reservoir model with an upscaled fault leakage function based on steady-state flow approximations. Here, faults are conceptualised as zones of increased vertical permeability in the caprock and reduced horizontal permeability in the reservoir. We integrate this rapid fault-leakage modelling framework with previous studies focused on geological screening and CO_2 storage site selection for the Malay Basin characterisation (de Jonge-Anderson et al., 2024a, 2024b, 2025a). It is applied to a predefined optimal storage zone in the Lower Miocene Group J aquifer, a sand-rich unit with high net-to-gross, elevated porosity and permeability, and complex faulting typical of mature Southeast Asian basins (de Jonge-Anderson et al., 2025a). The analysis combines deterministic sealing and leaking scenarios with a 10,000-realisation Monte Carlo uncertainty quantification across 71 parameters (fault permeability, capillary entry pressure, and transmissibility multiplier for each of 23 faults, plus reservoir porosity and permeability exponents). Spearman rank correlation quantifies the sensitivity of leakage outcomes to each parameter, and k-medoids clustering partitions the ensemble into distinct behavioural regimes with medoid scenarios available for detailed follow-up simulation. Conditional cluster probability analysis then identifies the parameter values at which regime membership shifts, translating the sensitivity ranking into useful site characterisation targets.

2 Geological Background

The Malay Basin is a 70,000 km^2 extensional basin located off the east coast of Peninsular Malaysia (Figure 1a). It has a long history of hydrocarbon exploration and production, with 14.8 billion barrels of oil equivalent produced from multiple reservoirs spanning its thick (up to 13 km) Cenozoic sedimentary fill (Madon, 2021). These characteristics have led to its identification as an attractive basin for CO_2 geological storage, with initial studies confirming gigatonnes of storage capacity across multiple aquifers and depleted hydrocarbon intervals (Hasbollah et al., 2020; Zhang & Lau, 2022; de Jonge-Anderson et al., 2025a).

This study specifically focuses on the Group J stratigraphic interval, selected based on its identification as a viable aquifer storage target in the regional GCS screening of de Jonge-Anderson et al. (2025a). It was deposited during the lower Miocene in shallow marine facies and consists of high-quality sandstone reservoirs. The aquifer represents one of the higher net-to-gross (NTG) sequences in the basin (de Jonge-Anderson et al., 2025a). Burial diagenesis significantly modifies reservoir properties, with porosity declining rapidly with depth, particularly within the uppermost 2000 m of burial. However, within optimal zones (< 3000 m burial depth), a median porosity of 18 % is maintained.

The Malay Basin is affected by pronounced faulting, particularly evident along the western margin hinge zone and central basin areas where north-south trending faults create extensive horst and graben systems that exert significant control over the depth structure and compartmentalisation of the basin fill (de Jonge-Anderson et al., 2024b). An *en-echelon* faulting pattern of overlapping curved faults affects the north of the basin. As a mature hydrocarbon province, the basin's faults have historically acted as effective seals for hydrocarbons over geological timescales, demonstrating inherent sealing capacity. However, seismic evidence indicates fault leakage in some locations (de Jonge-Anderson et al., 2024b), and deep-seated faults likely act as migration pathways for naturally occurring CO_2 (Madon et al., 2004). This study assesses the risk of CO_2 leakage along faults under injection conditions in this mature basin.

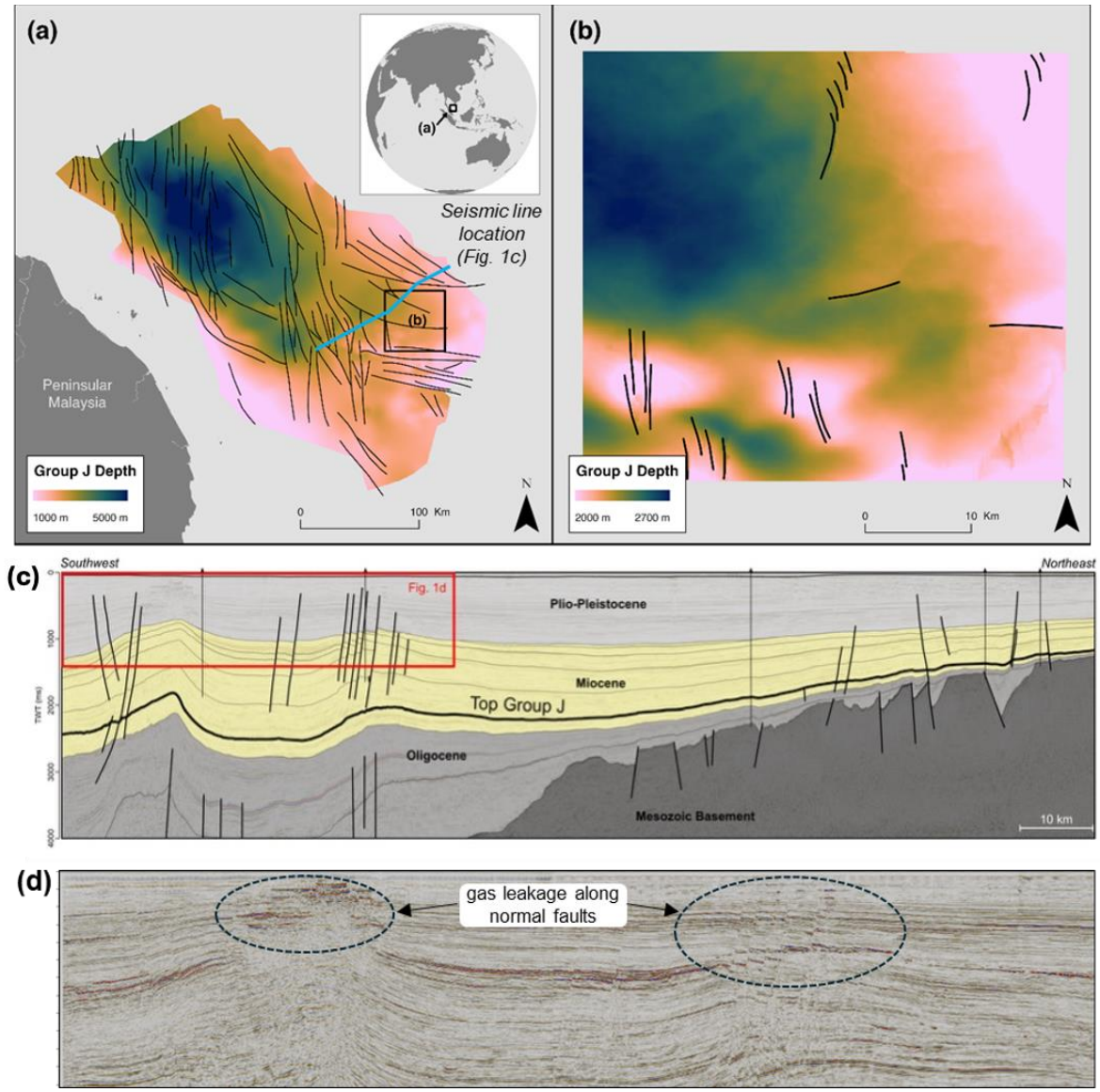

Figure 1 – Location maps of the Malay Basin and study area. (a) Regional depth map of the top Group J stratigraphic surface, constructed from horizon data and regional fault maps of de Jonge-Anderson (2025b) and PETRONAS (2022). (b) Local map of the study area at the eastern basin margin within the predefined optimal CO_2 storage zone; faults mapped from 3D seismic data as part of this study. (c) Regional structural cross-section adapted from de Jonge-Anderson et al. (2024b). (d) Seismic section showing acoustic anomalies consistent with vertical fluid migration.

3 Methods

3.1 3D Seismic Mapping

The area of interest lies at the southeast margin of the Malay Basin (Figure 1b). We used time-domain 3D seismic datasets to map a highly reflective and laterally continuous seismic reflector near the top of Group J. The horizon was gridded at 500 m cell resolution, then depth-converted using a generalized time-depth relationship from regional checkshot data (de Jonge-Anderson et al., 2024b). Faults were interpreted from visible offsets of the mapped horizon. The area slopes gently downdip to the northwest from approximately 2000 m in the east to around 2700 m in the west. In the south, a series of west-east oriented anticlines locally uplift Group J to approximately 2000 m. We constructed a simple 3D geological model from this mapped surface. The model top corresponds to the Group J surface, and the base was defined by duplicating this horizon and shifting it down by 100 m, representing the average Group J thickness in this area.

3.2 Reservoir Modelling

The reservoir modelling is based on fundamental equations governing fluid flow in porous media. The 3D mass conservation equation for two immiscible and incompressible fluid phases α, CO_2 (α = g) and brine (α = w) turn into a volume conservation equation

$$\frac{\partial(\phi s_\alpha)}{\partial t} + \nabla \cdot u_\alpha = q_\alpha, \tag{1}$$

where s_α is the saturation of phase α, ϕ is the porosity, u_α is the Darcy velocity of phase α, and q_α is a source/sink term in units of volume of phase α per time. The porous medium is assumed rigid and isothermal. The volume balance is established by

$$s_g + s_w = 1. \tag{2}$$

The Darcy velocity is given by

$$u_\alpha = -\frac{k_{r\alpha}}{\mu_\alpha} k(\nabla p_\alpha - \rho_\alpha \boldsymbol{g}), \tag{3}$$

where $k_{r\alpha}$ is the relative permeability, μ_α is the viscosity, k is the permeability tensor, ρ_α is the density, p_α is the fluid pressure (all for phase α), and $\boldsymbol{g}$ is the gravity acceleration vector. The phase pressures are related by the capillary pressure (p_c) function

$$p_c = p_g - p_w. \tag{4}$$

To obtain the fluid saturations and pressures by solving this system, three conditions must be met: firstly, specific functions must represent relative permeability and capillary pressure (Brooks-Corey functions used here); secondly, initial conditions for pressure and saturation throughout the reservoir domain must be established; and thirdly, appropriate boundary conditions must be defined.

3.3 Vertical Equilibrium Modelling

Vertical Equilibrium (VE) models exploit two fundamental characteristics of CO_2 storage systems: strong buoyancy contrast between CO_2 and brine, and large aspect ratio where lateral reservoir dimensions (hundreds of meters to kilometres) vastly exceed vertical dimensions (meters to tens of meters) (Huppert & Woods, 1995; Yortsos, 1995). These characteristics promote rapid vertical CO_2 segregation relative to lateral migration, establishing vertical hydrostatic equilibrium. Consequently, CO_2 accumulates as thin layers beneath low-permeability seals, and vertical pressure and saturation distributions

can be approximated by balancing buoyancy and capillary forces (Nordbotten & Celia, 2011).

VE models reduce problem dimensionality by vertically averaging the 3D conservation equations and Darcy's law, transforming the system into 2D governing equations solved on the lateral plane (Andersen et al., 2015; Nilsen et al., 2015). The approach preserves the standard multiphase Darcy equation structure, enabling implementation in conventional reservoir simulators and extension to incorporate additional physical phenomena including capillary hysteresis (Doster et al., 2013), residual trapping (Nilsen et al., 2016), and geomechanical coupling (Bjornara et al., 2016; Andersen et al., 2016, 2017). Post-simulation reconstruction recovers vertical pressure and saturation distributions from vertically integrated variables when detailed 3D fields are required. Benchmark studies comparing VE simulations against fully three-dimensional models for field-scale problems, including the Sleipner injection project, demonstrate comparable accuracy with orders-of-magnitude computational speedup (Nilsen et al., 2011, 2015, 2016; Bandilla et al., 2014; Moyner & Nilsen, 2019). We use a VE model implemented within the open-source software package MRST-co2lab, a module within the MATLAB Reservoir Simulation Toolkit (MRST) (Andersen, 2017; Lie, 2019). For comprehensive derivations and detailed treatment of VE assumptions and limitations, readers are referred to Nordbotten & Celia (2011). The simulation outputs are further used to identify an optimal injection well location through sequential filtering on overpressure, boundary connectivity, and CO_2 retention, as described in Section 4.1.3.

3.4 Upscaled Fault Leakage Function

The fault leakage modelling approach employs the analytical framework of Ramachandran et al. (2026), which estimates leakage rates using steady-state approximations. The fault is conceptualised as a permeable damage zone connecting the storage reservoir to an overlying aquifer (Figure 2). Following established understanding of fault zone architecture (Faulkner et al., 2010), the fault comprises a low-conductivity core surrounded by high-conductivity damage zones. The fault core acts as a barrier to across-fault flow within the reservoir, while the damage zones, containing fracture networks and deformation bands, permit upward fluid migration. For computational efficiency, the fault core is treated as impermeable (no-flow boundary), and the damage zone is modelled as an equivalent porous medium with representative bulk properties. This simplified representation provides a worst-case scenario for vertical leakage assessment. Hereafter, this damage zone is referred to as "the fault zone" or "the fault". Prior to CO_2 reaching the fault base, reservoir overpressure can drive brine leakage along the fault zone. The vertical brine leakage flux Q_{wf} is given as,

$$Q_{wf} = \begin{cases} 0, & h_g > 0 \\ \dfrac{A_f k_f}{\mu_w} \dfrac{(P_w - P_{w0})}{L_c}, & h_g = 0 \end{cases} \tag{5}$$

where A_f is the area of the fault perpendicular to flow, k_f is the vertical fault permeability, μ_w is brine viscosity, h_g is the CO_2 column height in the reservoir block connected to the fault block, P_w is the brine pressure in the reservoir, P_{w0} is the initial brine pressure in the reservoir, and L_c is the caprock thickness (i.e., the fault length connecting the storage reservoir to an overlying aquifer, assuming a vertical fault geometry for simplicity). Brine leakage occurs when the reservoir pressure exceeds the

initial pressure at the fault base, providing a pressure relief mechanism that reduces reservoir overpressure before it ceases once the CO_2 plume makes contacts. We assume that once the CO_2 plume contacts the fault base, the CO_2 plume forms a sufficiently thick layer that excludes the aqueous phase entry at low leakage rates (Kang et al., 2014).

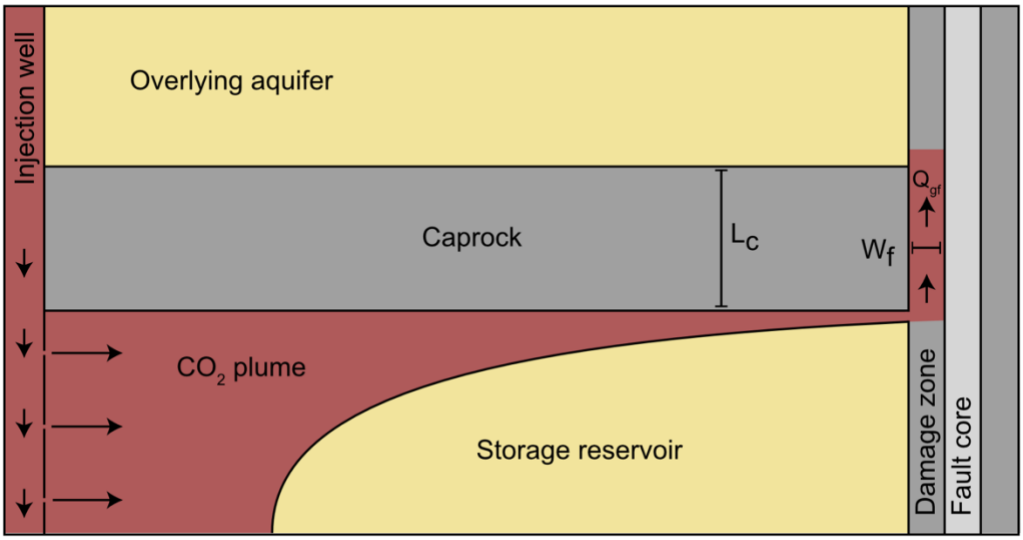

Figure 2 - Schematic vertical cross-section of a faulted storage reservoir showing fault architecture and leakage pathway. CO_2 leaks along the fault damage zone once it reaches the fault base within the reservoir. The fault core acts as a barrier to horizontal flow, while the damage zone permits vertical migration to a shallower overlying aquifer. Adapted from Ramachandran et al. (2026).

The along-fault leakage calculation adapts the analytical solution for flow through fissures between aquifers (Neufeld et al., 2009) to account for reservoir overpressure from injection and fault sealing capacity (Ramachandran et al., 2026). Fault seal capacity is controlled by capillary entry pressure (p_e), representing the threshold pressure required for CO_2 to invade the fault zone. The driving potential (ψ) is modelled as

$$\psi = \Delta\rho \boldsymbol{g} h_g + (P_w - P_{w0}) - p_e, \tag{6}$$

where $\Delta\rho = \rho_w - \rho_g$ is the density difference between brine and CO_2, and p_e is the fault capillary entry pressure. The first term represents buoyancy-driven flow, while the second term captures pressure-driven flow from injection-induced overpressure. CO_2 enters the fault base when $\psi > 0$, representing the capillary entry condition. Once entry is achieved, along-fault migration through the damage zone is governed by Darcy flow (Eq. 7). In the steady-state single-phase formulation adopted here, entry at the fault base and breakthrough at the fault top are treated as simultaneous: the $\Delta\rho \boldsymbol{g} L_c$ term in Eq. 7 represents the buoyancy head that builds as CO_2 traverses the fault zone of thickness L_c, such that the breakthrough pressure at the fault top is $p_e + \Delta\rho \boldsymbol{g} L_c$, consistent with laboratory measurements of capillary seal capacity (Busch & Amann-Hildenbrand, 2013; Espinoza & Santamarina, 2017). Higher capillary entry pressures delay leakage onset and reduce cumulative leakage volumes. The vertical gas leakage flux Q_{gf} along the fault is given as

$$Q_{gf} = \begin{cases} 0, & \psi \le 0 \\ \dfrac{A_f k_f}{\mu_g} \dfrac{(\psi + \Delta\rho \boldsymbol{g} L_c)}{L_c}, & \psi > 0 \end{cases} \tag{7}$$

where μ_g is the CO_2 viscosity. This approach relaxes the VE assumption at grid blocks connected to the fault, allowing non-zero vertical flow. However, for steady-state single-phase flow, fault leakage has a minimal effect on reservoir predictions (Kang et al., 2014). The fault leakage function is implemented as a source/sink term in the vertically integrated mass balance equations, avoiding explicit 3D fault discretisation. Grid cells containing faults have their across-fault permeability reduced using transmissibility multipliers or set to zero (representing the impermeable core) and incorporate the fault leakage function with specified properties. The steady-state single-phase assumption neglects transient accumulation within the fault. Although considerable, the impact of stress-sensitive permeability or fault reactivation is neglected here (Rutqvist, 2012; Rinaldi et al., 2014; Jha and Juanes, 2014; Vilarrasa et al., 2017; Zhao and Jha, 2019; Meguerdijian and Jha, 2021). These simplifications are acceptable for early-stage screening where the objective is bounding plausible leakage ranges rather than precise prediction. Full details on numerical implementation, verification, and sensitivity analyses are provided in Ramachandran et al. (2026).

3.5 Data Analysis and Clustering

Fault properties exhibit substantial uncertainty, especially during early-stage storage site assessment due to limited subsurface data. To quantify this uncertainty and identify parameter combinations controlling leakage behaviour, we employ Monte Carlo simulation with Latin hypercube sampling (McKay et al., 1979) combined with Spearman rank correlation analysis and k-medoids clustering. The uncertainty analysis samples 71 parameters independently: fault permeability, fault capillary entry pressure, and fault transmissibility multiplier for each of the 23 faults, plus reservoir porosity and permeability exponents. Fault properties follow log-uniform distributions spanning multiple orders of magnitude: k_f from 10^{-6} to 10^{-2} mD, p_e from 0.01 to 10 bar, and fault transmissibility multiplier from 10^{-6} to 10^{-1}. The exponents governing the porosity-depth and permeability-porosity relationships (Eq. 8 and 9) follow truncated normal distributions reflecting petrophysical relationships calibrated to basin data (de Jonge-Anderson et al., 2025a). Each fault is sampled independently to quantify fault-specific heterogeneity effects rather than assuming uniform properties across the fault system. Latin hypercube sampling ensures efficient parameter space coverage with fewer samples than random Monte Carlo methods while maintaining computational tractability. Spearman rank correlation analysis quantifies individual parameter sensitivity, selected for its robustness to non-linear relationships and log-distributed outcomes (Saltelli et al., 2007). For each parameter, the Spearman correlation coefficient between parameter value and total fault leakage identifies which faults and properties dominate system response.

K-medoids clustering partitions realisations into distinct behavioural regimes based on their positions in the parameter space. Unlike k-means clustering, which computes abstract centroids, k-medoids selects actual data points (medoids) as cluster representatives (Park & Jun, 2009). This distinction is critical for subsurface uncertainty analysis: medoids correspond to actual parameter combinations that can be extracted for detailed verification using computationally intensive 3D coupled simulations (Scheidt & Caers, 2009; Mahjour & Faroughi, 2023). Alternative approaches such as distance-based global sensitivity analysis (DGSA) identify influential parameter regions but do not produce specific testable scenarios. Several methods exist for determining the optimal number of clusters, including the elbow method, silhouette analysis, and the gap statistic

(Freites et al., 2023); the elbow method is used here, identifying the inflection point in within-cluster sum of squares versus cluster count. Unlike traditional sensitivity analysis that examines individual parameter influence, clustering reveals which parameter combinations define distinct leakage regimes, each encompassing a range of outcomes represented by a medoid scenario. This is a critical distinction because real-world leakage results from multi-parameter interactions rather than single-factor controls (Rinaldi et al., 2014; Gasda et al., 2022; Mahjour & Faroughi, 2023). The clustering identifies endmember scenarios representing best-case (minimal leakage) and worst-case (maximum leakage) outcomes, which can be extracted for detailed 3D numerical simulations without requiring full computational evaluation of the entire parameter space. Prior to clustering, all parameters are normalised using robust median-IQR (interquartile range) scaling: log-uniform fault parameters and total fault leakage are $\log_{10}$-transformed before scaling, whilst the normally distributed reservoir exponents are scaled on their original scale, ensuring comparable contributions to the Euclidean distance metric. Total fault leakage is included as an additional variable with a weight of 2, ensuring that cluster boundaries reflect leakage behaviour rather than parameter-space proximity alone.

To characterise the functional relationship between individual parameters and leakage regime membership, we compute the conditional cluster probability $\mathrm{P}(\mathrm{cluster}|\mathrm{x})$ for each of the top 15 parameters ranked by spearman correlation coefficient. For each discrete bin along the parameter's sampled range, conditional cluster probability is estimated as the fraction of all realisations falling within that bin that were assigned to a given cluster. Bin edges are defined uniformly across the full ensemble range of each parameter using 20 equal-width intervals, with a minimum occupancy threshold of 10 realisations per bin applied to suppress unreliable estimates at sparse distribution tails. The unconditional cluster fractions, defined as the fraction of all realisations assigned to each cluster irrespective of any single parameter value, serve as the null baseline. A parameter with no discriminating power produces conditional probability curves that coincide with these baselines across its full sampled range.

Together, these methods translate a high-dimensional uncertainty quantification into actionable site characterisation targets: rather than requiring comprehensive characterisation across all 71 parameters, the sensitivity ranking and conditional probability analysis identify the small subset of faults whose properties are most critical to storage outcomes. These are the few faults, among the many, that warrant targeted characterisation. This targeted approach is particularly valuable at early-stage screening, where full-physics 3D coupled simulations are computationally prohibitive across the full parameter space.

4 Results

4.1 Well Location Identification Under Fault Uncertainty

4.1.1 Model Parameters

The model is applied to a section of Group J in the Malay Basin, as illustrated in Figure 3. Key geological and operational parameters are listed in Table 1, including a seafloor depth of 70 m below sea level, an average top reservoir depth of 2300 m below the seafloor, a geothermal gradient of 50 °C.km^{-1}, and a seafloor temperature of 24 °C (Madon & Jong, 2021; de Jonge-Anderson et al., 2025a). Rock compressibility is applied to the reservoir formation only; the value adopted here is from de Jonge-Anderson et al. (2024a)

for a neighbouring field within the Malay Basin. The reservoir model has a grid resolution of 500 m x 500 m (Figure 3). The porosity (ϕ) and permeability (k) across the grid are obtained from de Jonge-Anderson et al., (2025a), where porosity is calculated as a function of depth (z) and permeability is derived from porosity (Eq. 8 and 9; Figure 4).

$$\phi = 0.45e^{(-a_1 z)} \quad (8)$$

$$k = 700236\phi^{b_1} \quad (9)$$

where a_1 (10th/median/90th percentile = 3.83 x 10^{-4}/5.34 x 10^{-4}/6.84 x 10^{-4}) follows a truncated normal distribution (mean = 5.34 x 10^{-4} and standard deviation = 2.15 x 10^{-5}), and b_1 (10th/median/90th percentile = 3.47/4.05/4.63) follows a truncated normal distribution (mean = 4.05 and standard deviation = 8.22 x 10^{-2}). Section 4.1 uses median values for deterministic fault location, while Section 4.2 employs the distributions for uncertainty quantification. Permeability (k) is in millidarcies (mD). Fault width is fixed at 5 m, representative of faults with 10 - 100 m displacement in clastic settings (Childs et al., 2009; Torabi & Berg, 2011). Because damage-zone width enters the upscaled leakage function as a product with fault permeability (Eq. 7), uncertainty in width is implicitly subsumed within the sampled fault permeability.

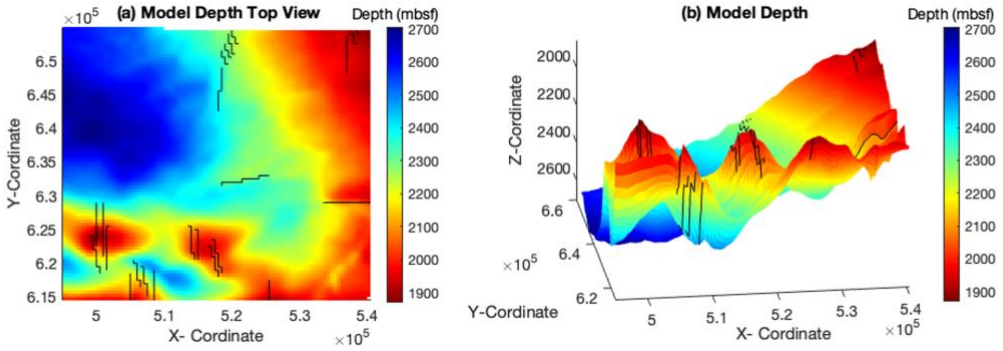

Figure 3 - Depth structure of the Group J top surface. (a) 2D map showing the spatial variation in depth. The colour scale represents depth from deep (blue) to shallower (red). Black lines show the 24 mapped faults. (b) 3D surface plot showing the topographical distribution. The z-axis represents the depth. Both visualisations reveal significant depth variations, with shallower regions in the central and northeastern portions and a structural depression in the southwest.

We explicitly define 23 distinct faults in Figure 3, with fault coordinates identifying the corresponding grid faces that act as fault boundaries. The upscaled fault leakage function as defined in Section 3.4 is integrated into these cells to account for fluid flow vertically along the fault. We assume a saline aquifer setting, where the initial reservoir pressure is set as hydrostatic, and the reservoir is fully saturated with brine. All simulations use a single injection well with an injection rate of 1 Mt per year for 30 years followed by a 970-year post-injection period, with open boundaries maintained at hydrostatic conditions. Total fault leakage is reported as the cumulative CO_2 flux that has broken through to the overlying aquifer at the fault top.

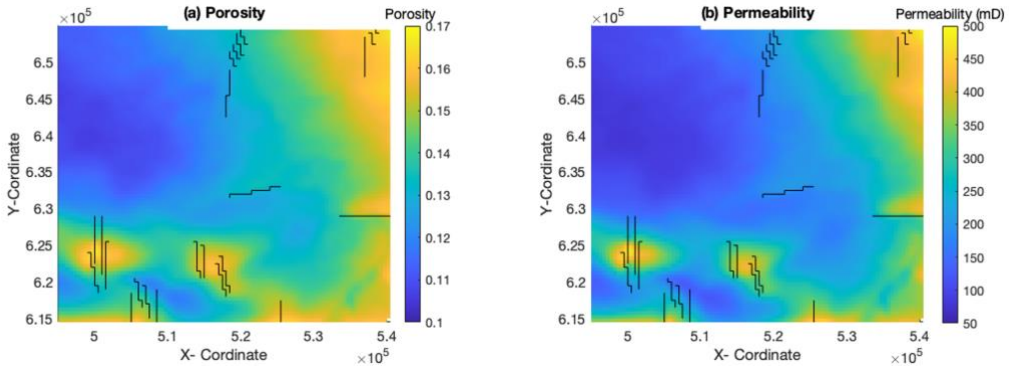

Figure 4 - Spatial distribution of reservoir properties calculated from depth. Black lines show the 24 mapped faults. (a) Porosity distribution ranging from 0.05 to 0.18. (b) Permeability distribution ranging from 100 to 550 mD. Both properties were calculated as functions of depth using petrophysical relationships shown in Eq. 8-9. The correlation between porosity and permeability distributions assumes depth-controlled diagenetic processes influencing reservoir characteristics (de Jonge-Anderson et al., 2024b).

Table 1 – Model parameters for Group J reservoir simulation in the Malay Basin. Porosity and permeability relationships (Eqs. 8-9) are from de Jonge-Anderson et al. (2025a). Fault parameters shown here represent the baseline Case A (sealed faults); variable fault properties for Cases A and B are given in Table 2.

Property	**Values**
Cell Dimensions (DX*DY) (m)	500 x 500
Cell thickness (DZ) (m)	100
Average top reservoir depth (m) (z)	2300
Rock compressibility (Pa^{-1})	4.35×10^{-10}
Seafloor temperature (°C)	24
Temperature gradient (°Ckm^{-1})	50
Seafloor Depth (m)	70
Brine viscosity (Pa.s)	3.13×10^{-4}
CO_2 viscosity (Pa.s)	3.21×10^{-5}
Brine density (kgm^{-3})	1001.0
CO_2 density (kgm^{-3})	420.0
Fault (damage zone) permeability (mD)	See Table 2
Fault (damage zone) width (m)	5
Caprock thickness (m)	500
Fault (damage zone) Capillary Entry Pressure (bar)	See Table 2
Residual gas saturation (Reservoir)	0.2
Irreducible brine saturation (Reservoir)	0.3

Table 2 – Fault property scenarios for well location analysis. Case A (sealed) represents structural containment with no fault leakage. Case B (leaking) represents compromised fault sealing with both vertical leakage along faults and reduced lateral sealing.

Case	**Fault Capillary Entry Pressure (p_e) (bar)**	**Fault Permeability (k_f) (mD)**	**Fault Transmissibility Multiplier**
Case A	∞	0	0
Case B	0.05	10^{-3}	0.01

4.1.2 Scenario Definitions

We analyse two scenarios to assess the impact of fault sealing capacity on storage performance (Table 2). Case A represents fully sealing faults where both horizontal (across-fault) and vertical (along-fault) flow are completely blocked, establishing the upper bound for CO_2 retention. Case B represents leaking faults with properties reflecting compromised sealing capacity: fault permeability of 10^{-3} mD (vertical flow along damage

zone), capillary entry pressure of 0.05 bar (reduced resistance to CO_2 entry), and transmissibility multiplier of 0.01 (across-fault flow reduced to 1% of reservoir permeability). In natural fault systems, damage zone width, permeability, and capillary entry pressure are systematically related to fault displacement (Caine et al., 1996; Childs et al., 2009; Faulkner et al., 2010). For this illustrative comparison, we assume uniform fault properties across all 23 mapped faults. While this assumption is geologically simplistic, it enables clear demonstration of how fault sealing capacity influences migration patterns and storage security. Section 4.2 relaxes this assumption by treating fault properties as uncertain parameters with spatially variable distributions.

4.1.3 Results

Figure 5 presents the baseline scenario where all faults are fully sealing in both horizontal and vertical direction. CO_2 retention is defined as the total injected mass minus cumulative boundary losses and fault leakage after 1000 years. Under Case A, lateral boundary loss is the sole mechanism of CO_2 loss from the system. Retention varies spatially across the 600 well locations (Figure 5a), controlled primarily by proximity to domain boundaries and structural position. Wells placed within fault-bounded compartments or in downdip structural depressions achieve higher retention than boundary-proximal locations. Maximum overpressure (pressure above the initial hydrostatic pressure) remains below 4 MPa across all well locations (Figure 5b), indicating that injection at 1 Mtpa does not approach pressure limits that would constrain operations at this site. The northeastern region, the deepest and least permeable part of the domain (~50 mD and 10% porosity), experiences the highest overpressure despite low retention. This is because, in low-transmissivity settings, reduced lateral pressure dissipation results in localised pressure build-up.

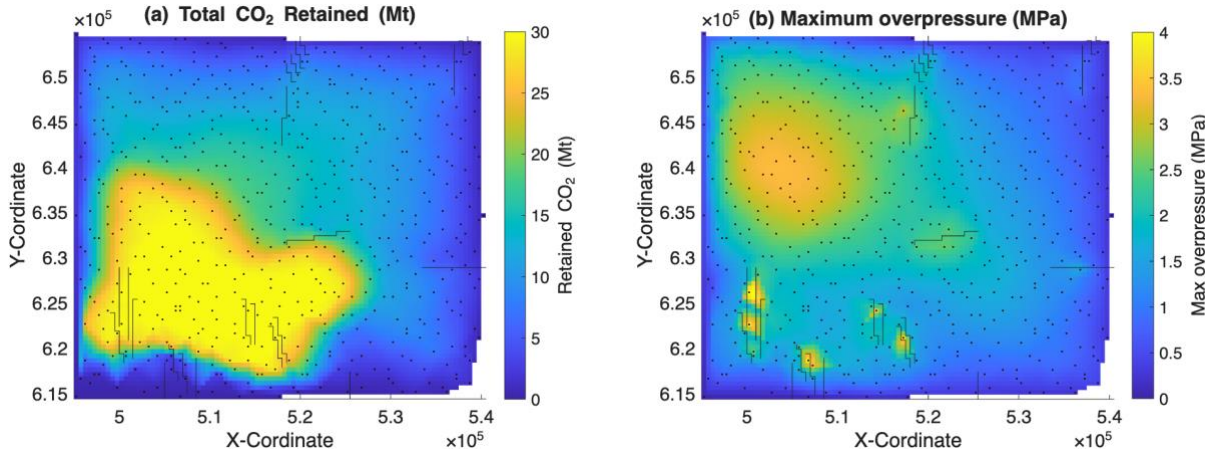

Figure 5 – Spatial distribution of CO_2 retention and pressure buildup under Case A (sealed faults baseline). (a) Total CO_2 retained after 1000 years for 600 simulated well locations (red dots), computed as total injected mass minus boundary losses and fault leakage. Faults (black lines) are fully sealing both laterally and vertically. High retention zones (warm colours) indicate locations with optimal structural containment, while low retention zones (cool colours) represent areas with greater lateral boundary losses. (b) Maximum overpressure above initial hydrostatic pressure observed anywhere in the reservoir over the 1000-year simulation period for the specific well location. All locations remain below 4 MPa, indicating pressure buildup stays within safe operational limits at 1 Mtpa injection rate.

Figure 6 examines the same well locations under compromised fault sealing conditions (Case B). CO_2 retention (Figure 6a) shows spatially variable reduction relative to Case A, with losses concentrated near faults intercepting the plume migration pathways. The

southwestern structural depression, bounded by major fault zones, limits lateral connectivity to domain boundaries, maintaining higher retention than locations with direct updip pathways to domain boundaries. Maximum overpressure (Figure 6b) exhibits similar spatial distribution to Case A, with peak values remaining below 4 MPa. CO_2 leakage along faults (Figure 6c) reaches up to 0.3 Mt (~ 1% of injected mass) in locations where plumes directly contact faults, concentrated in the central and northern portions of the domain where structural dip drives updip migration toward faults. Brine leakage along faults (Figure 6d) precedes CO_2 plume arrival, driven by injection-induced overpressure at the fault base. Cumulative brine leakage reaches up to 2 Kt, approximately 150 times below the maximum CO_2 leakage of 0.3 Mt. This early brine leakage is nonetheless physically meaningful: the associated pressure dissipation at the fault reduces the injection-induced overpressure driving force (Eq. 6) when CO_2 subsequently contacts the fault.

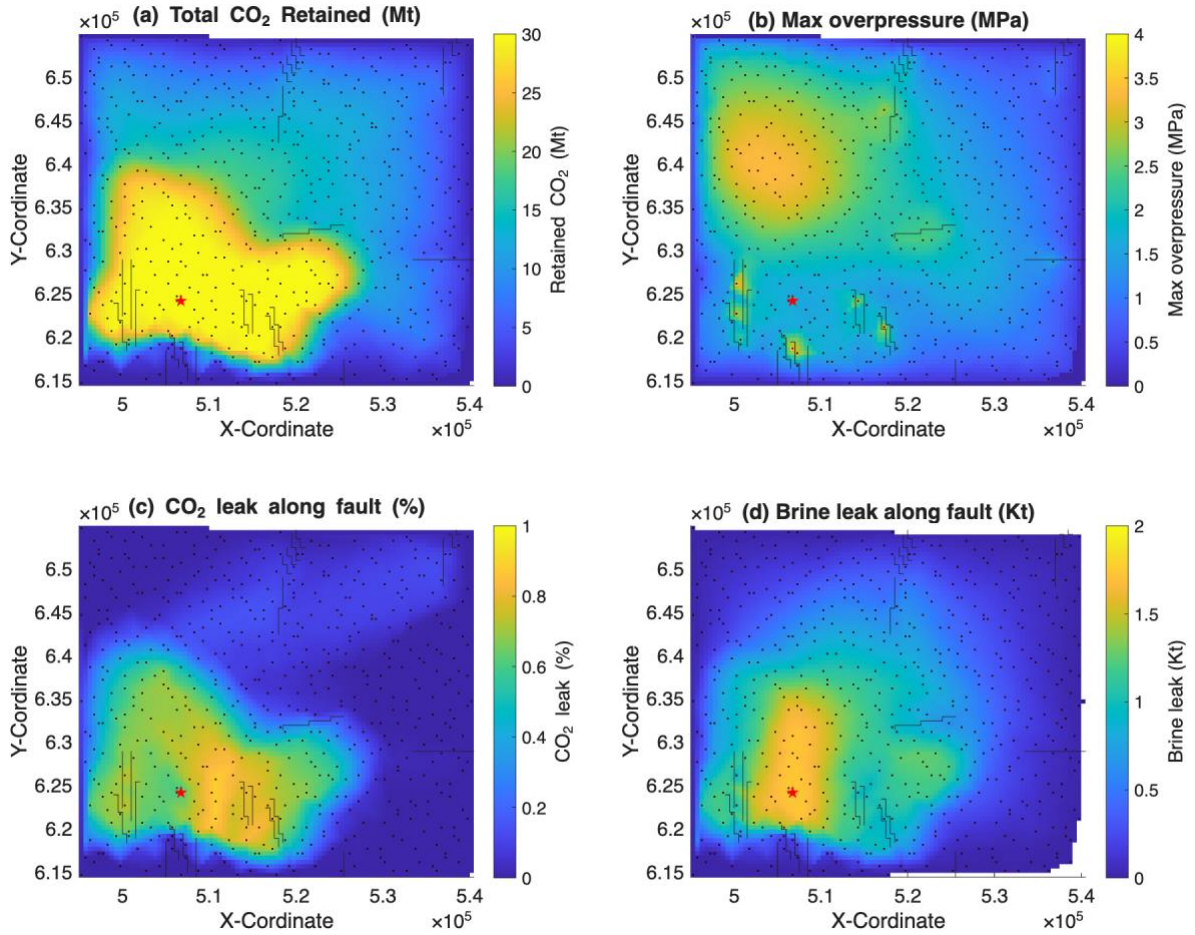

Figure 6 – Spatial assessment of CO_2 retention and fault leakage under Case B (leaking faults scenario). (a) Total CO_2 retained after 1000 years shows reduced retention compared to Case A. (b) Maximum overpressure distribution remains similar to Case A. (c) Cumulative CO_2 leakage along faults reaches up to 1% (0.3 Mt), concentrated where plumes migrate updip and contact fault planes. The cumulative leak is divided by the total injected to arrive at the percentage value shown here. (d) Cumulative brine leakage along faults reaches up to 2 Kt, driven by early-time injection-induced overpressure before CO_2 plume arrival. Red star marks the optimal location [506750, 624150], selected by sequential filtering on overpressure, boundary connectivity, and CO_2 retention. Black lines show faults; red dots show 600 well locations.

The optimal well location is identified using a sequential filtering approach. First, locations where maximum overpressure exceeds 2 MPa are excluded; this threshold is set as a conservative screening-stage proxy for geomechanical risk, set at half the maximum overpressure observed (Figure 6b); site-specific stress characterisation is required to define a geomechanically rigorous pressure limit. Second, locations where CO_2 migrates across the open model domain boundaries are excluded, as lateral boundary loss implies that containment depends on structural or hydraulic features outside the modelled domain. The remaining locations are ranked by CO_2 retention fraction (total injected mass minus boundary losses and fault leakage, normalised by total injected mass) after 1000 years, and the top-ranked location at coordinates [506750, 624150] is selected (red star, Figure 6). This location sits within the southwestern structural depression between two major fault zones, where structural compartmentalisation limits lateral connectivity to domain boundaries. Cross-referencing with Figure 4 reveals this region exhibits slightly higher porosity (~12-15%) and permeability (~300-400 mD). Storage patterns show a systematic decrease towards boundaries due to lateral migration across model boundaries. This structural depression provides favourable storage conditions despite being shallower than the deepest portions located in the northeastern part of the model domain. Locations near multiple fault intersections or in shallow updip positions show increases in leakage risk under Case B conditions (Figure 6c).

4.2 Uncertainty Analysis

4.2.1 Spearman Sensitivity Analysis

Unlike the deterministic Cases A and B that assumed uniform fault properties across all 23 faults, real fault systems exhibit heterogeneous sealing capacity controlled by spatially variable permeability, capillary entry pressure, and transmissibility. To quantify the influence of fault-specific heterogeneity on leakage risk, we conducted 10,000 Monte Carlo simulations using Latin hypercube sampling across 71 uncertain parameters: 23 fault permeability values, 23 fault capillary entry pressure values, 23 fault transmissibility multipliers, plus reservoir porosity and permeability exponents (Table 3). Fault properties were sampled independently for each fault from distributions spanning the ranges shown in Table 3. This permeability range (10^{-6} to 10^{-2} mD, equivalent to 10^{-21} to 10^{-17} m^2) spans effectively unfractured caprock conditions at the lower bound to well-connected fractured damage zones at the upper bound, consistent with effective damage zone permeabilities derived from single-fracture stress-permeability relationships and fracture density distributions at natural CO_2 leakage sites (Snippe et al., 2022). Each simulation tracked CO_2 remaining in the reservoir, lateral boundary losses, and cumulative fault leakage over 1000 years. For each of the 71 parameters, we calculated the Spearman correlation coefficient (r_s) between the parameter value and total fault leakage across all 10000 realisations. Figure 7 presents the spatial distribution of fault sensitivity alongside a composite ranking of all parameters.

Table 3 - Parameter distributions for uncertainty analysis. Fault parameters sampled independently for each of 23 faults. All fault properties follow log-uniform distributions; reservoir exponents (porosity and permeability) follow truncated normal distributions. All other parameters match Table 1.

Property	Distribution	Low Values	High Values
Fault permeability (mD) (x23)	Log-Uniform	10^{-6}	10^{-2}
Fault capillary entry pressure (bar) (x23)	Log-Uniform	0.01	10
Fault transmissibility multiplier (-) (x23)	Log-Uniform	10^{-6}	10^{-1}

Reservoir porosity exponent (-)	Truncated-Normal	0.000383	0.000684
Reservoir permeability exponent (-)	Truncated-Normal	3.4749	4.6264

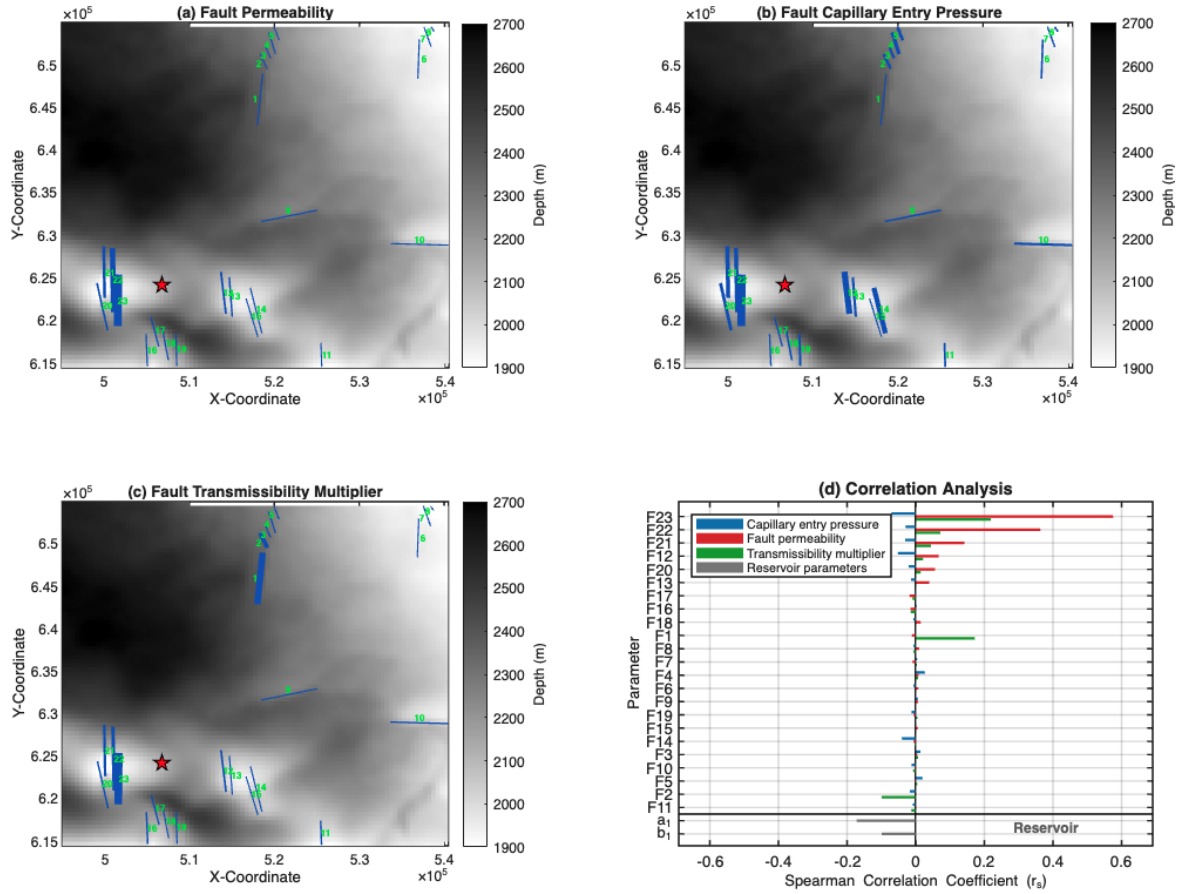

Figure 7 - Fault-specific sensitivity analysis from 10,000 Monte Carlo realisations. (a-c) show fault locations coloured and weighted by Spearman correlation coefficient with total fault leakage for permeability, capillary entry pressure, and transmissibility multiplier respectively. The fault is represented here in blue where the line thickness scales with correlation coefficient. Red star marks injection well location. Greyscale background is used to maximise contrast with fault line thickness, which scales with Spearman correlation coefficient. (d) presents composite correlation ranking for all 71 parameters, with faults sorted by correlation coefficient for fault permeability and reservoir parameters shown below.

Leakage sensitivity concentrates on a small fault subset. Only 5 of 23 faults (Faults 23, 22, 21, 12, and 20) exhibit Spearman coefficients for the fault permeability > 0.05 against total leakage (Figure 7). These five faults represent 22% of the fault population yet dominate system uncertainty, providing a clear target where further site characterisation and data acquisition are needed to constrain uncertainties. Within this updip subset, Fault 23 exhibits the strongest sensitivity, approximately 5-10 times larger than the next most influential faults. The spatial pattern of influential faults reflects CO_2 migration pathways controlled by structural geometry and injection location. Faults 20-23 lie in the southwestern updip region close to the injection well (Figure 7a), positioned along the plume migration pathway where CO_2 accumulates at structural highs. These faults intercept migrating CO_2 and exhibit strong positive correlation with permeability and transmissibility, confirming that their hydraulic conductivity controls leakage rates once CO_2 contact occurs. In contrast, faults distant from the well show negligible influence on total leakage despite spanning the same parameter ranges. Reservoir properties exhibit

negligible correlation with fault leakage, approximately 3-6 times weaker than the dominant fault sensitivities (Figure 7d).

Faults further away from the injection well show relatively stronger negative correlation with capillary entry pressure than nearby faults despite contributing less to total leakage. For example, Fault 12 (distant, northern position) exhibits $r_s(p_e)$ = -0.053 compared to Fault 23's $r_s(p_e)$ = -0.071, despite Fault 23's permeability correlation being 9 times stronger. This distance-dependent sensitivity reflects the diminishing pressure drive with distance from the injection well: in farther locations where overpressure is small, capillary entry pressure becomes the primary control on whether leakage takes place, whereas near-well faults are already breached in most realisations, as elevated injection-induced overpressure exceeds the capillary entry pressure regardless of its sampled value.

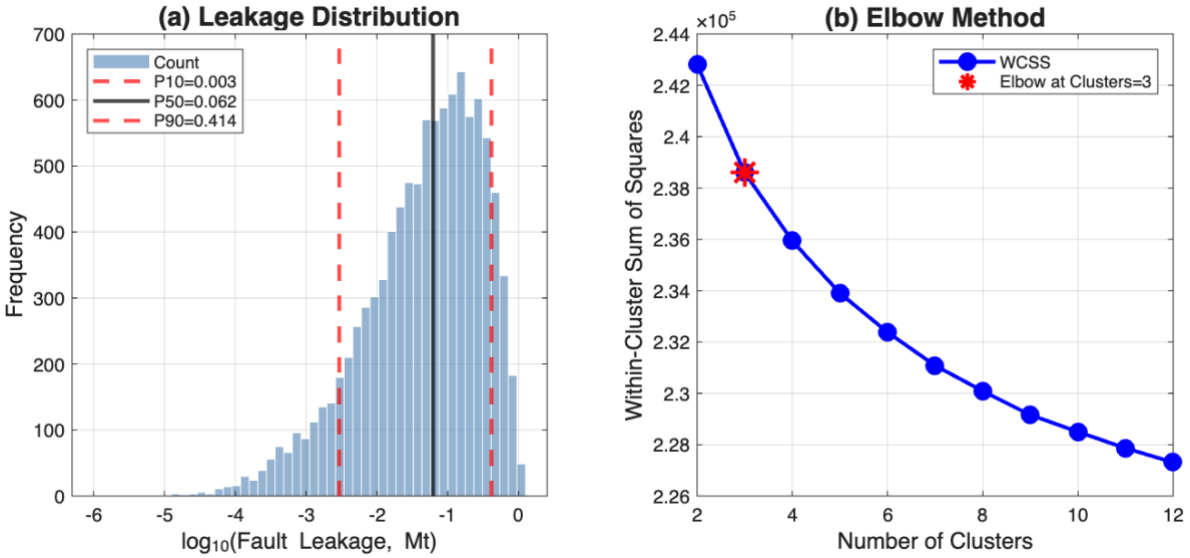

Figure 8 – (a) Probability distribution of total fault leakage after 1000 years from 10,000 Monte Carlo realisations. Vertical lines mark P10 (0.003 Mt), P50 (0.062 Mt), and P90 (0.414 Mt) quantiles. (b) Elbow method showing within-cluster sum of squares versus number of clusters, with optimal selection at 3 marked with a red star.

Unlike the other faults with significant Spearman correlation, which are controlled by fault permeability and capillary entry pressure as CO2 migrates updip and leaks along the fault zone, Fault 1 is controlled by its transmissibility multiplier. Although Fault 1 permeability shows minimal correlation with total fault leakage, its transmissibility multiplier exhibits substantial positive correlation with total fault leakage, ranking second among all faults for this parameter. This transmissibility dominance indicates Fault 1 functions as a "gateway fault": when its across-fault transmissibility is high, CO_2 can migrate laterally through the fault zone and access the northern fault array (Faults 2-5), creating cascading leakage pathways. When Fault 1 maintains low transmissibility, it isolates the northern domain, preventing CO_2 from reaching downstream faults regardless of their individual properties. This finding cannot be identified through simple single-fault sensitivity analysis and demonstrates the value of comprehensive multi-fault uncertainty quantification.

4.2.2 Leakage Clustering Analysis

Total fault leakage after 1000 years spans approximately two orders of magnitude from P10 = 0.003 Mt (0.01% of injected mass) to P90 = 0.414 Mt (1.4% of injected mass) (Figure

8a). The median leakage of 0.062 Mt represents 0.21% of total injected CO_2. However, the upper tail of the distribution reaches P90 = 0.414 Mt, equivalent to 1.4% of injected mass, demonstrating that unfavourable combinations of fault properties can produce elevated leakage. The distribution exhibits strong positive skewness on a linear scale, with approximately 35% of realisations producing near-zero leakage (< 0.01 Mt) while less than 10% exceed 0.2 Mt. This asymmetry indicates that high-leakage outcomes require specific combinations of fault properties rather than random parameter variations, motivating clustering to identify the parameter combinations governing distinct leakage regimes.

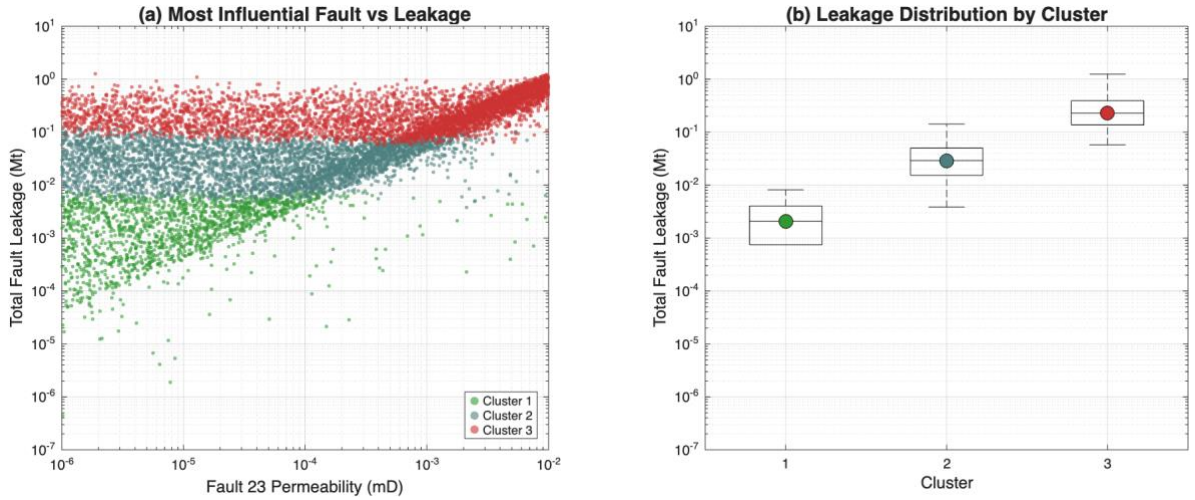

Figure 9 - Cluster optimization and characterisation. (a) Scatter plot of total fault leakage versus Fault 23 permeability (most influential fault) coloured by cluster assignment, demonstrating clear regime separation. (b) Box plots showing leakage distribution by cluster, with median values marked.

K-medoids clustering partitions the 10,000 realisations into distinct behavioural regimes based on their positions in the 71-dimensional parameter space. The optimal number of clusters was determined using the elbow method (Figure 8b). The elbow occurs at cluster = 3, yields physically interpretable regimes (low, moderate, high leakage).

Cluster 1 (low-leakage regime, n=1652, 16.5%) shows median leakage of 0.002 Mt (P10=0.0003, P90=0.006 Mt). Cluster 2 (moderate-leakage regime, n=3940, 39.4%) shows median leakage of 0.03 Mt (P10=0.010, P90=0.070 Mt). Cluster 3 (high-leakage regime, n=4408, 44.1%) shows median leakage of 0.230 Mt (P10=0.099, P90=0.588 Mt). The progression between clusters represents an ~15-fold increase from Cluster 1 to Cluster 2 and a ~8-fold increase from Cluster 2 to Cluster 3. The clear separation between regimes in leakage space reflects both the structure of the parameter distributions and the outcome-oriented weighting applied in the distance calculation (Section 3.5); the qualitative three-regime structure is expected to be robust to moderate changes in weighting, but the precise boundaries between clusters are conditioned on this choice. High-leakage scenarios (Cluster 3) represent the modal outcome, containing 44.1% of realisations compared to 16.5% in the low-leakage regime. Under current parameter uncertainty, elevated leakage is the single most probable outcome, exceeding the moderate-leakage regime by five percentage points. Cluster membership is predominantly controlled by a single fault (Fault 23) rather than distributed across the 23-fault system. Analysis of cluster-conditional parameter distributions for the top five influential faults (Faults 23, 22, 21, 12, 20) reveals that Fault 23 permeability exhibits a

~100-fold difference between low and high-leakage clusters, substantially exceeding the differences observed for other faults (35x for Fault 22, declining to 1.7x for Fault 20). The visual separation of clusters in Fault 23 permeability space (Figure 9a) demonstrates that this single parameter serves as an effective proxy for regime classification. The low-leakage regime requires restrictive parameter combinations rather than simply avoiding unfavourable values. Cluster 1 scenarios simultaneously maintain low permeability across multiple updip faults (Faults 20-23) combined with elevated capillary entry pressures, a narrow subset of the sampled parameter space.

Fault capillary entry pressure shows secondary influence on cluster assignment compared to fault permeability. For the top five influential faults, the ratio of median fault capillary entry pressure is 16–42% lower in the high-leakage cluster than in the low-leakage cluster, indicating modest variation compared to the orders-of-magnitude differences in permeability. This pattern is consistent with the correlation analysis showing that capillary effects dominate in pressure-limited environments distant from the injection well, whereas permeability controls leakage rates in the near-well region where pressure drive remains elevated.

4.2.3 Conditional Cluster Probability

Figure 10 presents the conditional cluster probability for the top 15 parameters ranked by Spearman correlation coefficient, showing the fraction of realisations in each leakage regime as a function of parameter value. Dashed lines mark the unconditional cluster fractions (C1: 16%, C2: 39%, C3: 44%); deviation from these baselines quantifies the information each parameter value provides about leakage regime membership. Figure 10 identifies not only which parameters dominate leakage uncertainty, but what values they need to take to shift cluster membership. Parameters whose curves deviate strongly from the unconditional baselines are those for which a single measurement would substantially resolve the current uncertainty; the crossing point where respective cluster probability equals the unconditional fraction marks the threshold value separating predominantly favourable from predominantly unfavourable outcomes.

Fault 23 permeability shows a response concentrated at the upper end of the sampled range. Above approximately 10^{-3} mD, Cluster 3 conditional probability rises well above the unconditional fraction of 0.44, approaching 0.9 near the upper bound. Below 10^{-3} mD, this falls below 0.44 but does not approach zero, because Fault 22 permeability and Fault 1 transmissibility can independently drive high-leakage outcomes. The crossing point near 10^{-3} mD therefore marks the value above which Fault 23 permeability alone indicates elevated leakage risk, providing a concrete characterisation target that the Spearman correlation coefficient-based ranking alone cannot supply. Fault 1 transmissibility shows a different character: Cluster 3 conditional probability increases gradually from approximately 0.35 to 0.60 across the full sampled range without a sharp crossing point, indicating that no single measurement value decisively shifts cluster membership. Instead, any reduction in transmissibility uncertainty progressively narrows the probable leakage regime, consistent with its role as a gradual control on CO_2 access to the northern fault array rather than an on/off sealing threshold. For the remaining parameters in the ranking, conditional probability curves show progressively smaller deviations from their unconditional baselines, confirming that below the top five (Fault 23 permeability, Fault 22 permeability, Fault 23 transmissibility, Fault 1 transmissibility, and the porosity exponent a_1), individual parameter values provide little additional information about leakage regime membership beyond the prior.

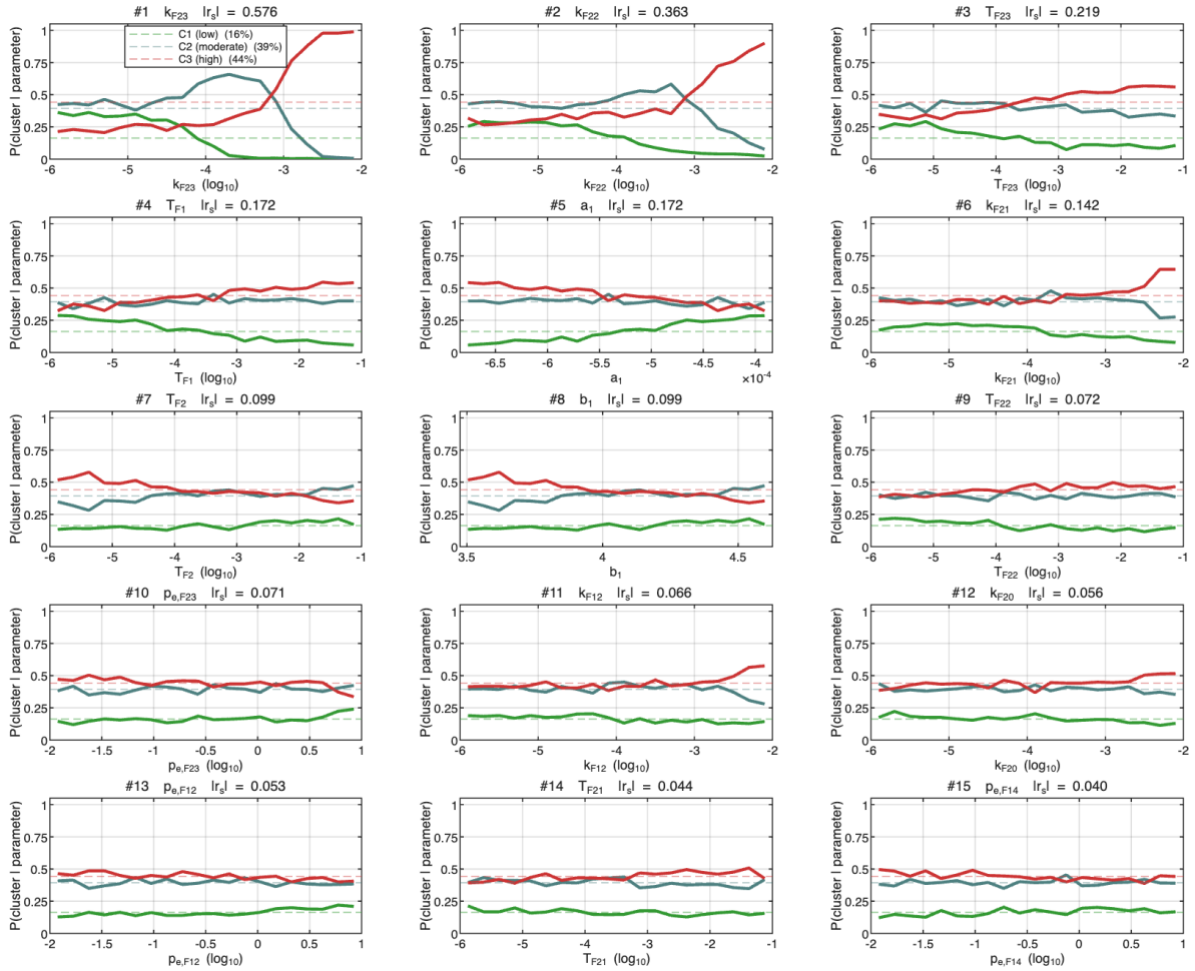

Figure 10 – Conditional cluster probability for the top 15 parameters ranked by Spearman coefficient. Each panel shows conditional probability as a function of the parameter, where the y-axis is probability (0–1) and the three solid lines (green: C1 low leakage, teal: C2 moderate leakage, red: C3 high leakage) sum to 1 at every x-value. Fault properties are plotted on a $\log_{10}$ axis; reservoir exponents (a_1, b_1) on a linear axis. Dashed lines indicate unconditional cluster fractions (C1: 16%, C2: 39%, C3: 44%), representing the probability prior to observing any parameter value. Solid-line deviation from the dashed baseline quantifies the discriminating power of each parameter: strong deviation indicates a high-value characterisation target; coincidence with the baseline indicates negligible influence on leakage regime.

The clustering identifies three medoid scenarios representing physically realisable parameter combinations for each regime. These medoid realisations can be extracted for detailed simulations, enabling assessment of effects neglected here without requiring full computational evaluation of the entire ensemble with 10,000 realisations. The conditional cluster probability analysis extends this further, identifying the specific parameter values at which cluster membership shifts and translating the correlation ranking into concrete characterisation targets. Together, the correlation, clustering, and conditional probability analyses shift risk assessment from parameter sensitivity analysis to scenario identification, enabling site selection that balances operational targets against geological constraints rather than applying blanket exclusion criteria.

5 Discussion

Structurally complex faulted basins have historically been regarded with caution as CO_2 storage targets, yet the present results suggest that quantitative risk screening can

reframe this perception. Such basins were deprioritised due to perceived leakage risks. Natural CO_2 accumulations show both outcomes at faulted sites: Bravo Dome and St Johns Dome have retained large CO_2 volumes over geological timescales despite active faulting, while fault-focused surface seepage has been documented at Green River, Utah, where CO_2 migrates along normal fault damage zones (Miocic et al., 2019a, 2019b; Snippe et al., 2022). The same framework is applicable to subseismic faults that lie below seismic resolution; their potential presence and properties can be incorporated as additional uncertain parameters within the Monte Carlo framework, enabling leakage risk to be bounded where fault mapping is incomplete. The coexistence of these outcomes across mapped and potentially unmapped fault populations suggests that faulted basins are not uniformly unsuitable for storage; quantitative fault characterisation represents a more appropriate early-stage response than blanket avoidance.

Well placement in faulted storage systems requires balancing structural confinement against pressure management constraints. Pressure propagation extends far beyond the CO_2 plume at basin scale (Birkholzer & Zhou, 2009; Zhou & Birkholzer, 2011), and pressure space, the capacity of connected formations to absorb injection-induced overpressure without triggering fault reactivation or injectivity loss, is increasingly recognised as the primary limitation on storage scalability (Birkholzer & Zhou, 2009; Bump & Hovorka, 2024; Ougier-Simonin et al., 2026). Well placement optimisation and brine extraction strategies have been proposed to address this constraint (Cihan et al., 2015; González-Nicolás et al., 2019), with recent work extending to fault slip minimisation as an explicit objective (Raji et al., 2025) and to basin-scale pressure assessment in multi-fault systems (Cihan et al., 2026). The sequential filtering approach applied here addresses the same coupled problem at early screening stage: in this study, overpressure and boundary connectivity together constrain the viable well location space more effectively than optimising on CO_2 retention alone, with the southwestern structural depression emerging as the preferred location. This structural depression warrants further characterisation, as fault-bounded compartmentalisation limits lateral connectivity while maintaining adequate transmissivity for pressure dissipation (Zhou et al., 2008; Mears et al., 2026). This result is consistent with observations that structural position and boundary conditions collectively control effective storage volumes in compartmentalised systems (Mhlambi et al., 2025), and that low-transmissivity settings can simultaneously constrain injectivity and amplify local pressure buildup (de Jonge-Anderson et al., 2026).

The dominant influence of fault permeability and capillary entry pressure on leakage outcomes carries a direct implication for characterisation programme design that extends beyond the simple observation that both parameters are uncertain. Capillary entry pressure governs the onset threshold for vertical CO_2 flow: faults with sufficiently elevated entry pressure remain effectively sealing even under injection-induced overpressure, because the combined buoyancy and pressure driving potential cannot overcome the capillary resistance at the fault base (Espinoza & Santamarina, 2017; Busch & Kampman, 2018). The relative importance of entry pressure and permeability is not, however, spatially uniform. Faults in close proximity to the injection well, in our simulations, experience injection-induced overpressure sufficient to breach capillary resistance across a wide range of entry pressure values, placing permeability as the dominant control on leakage magnitude in this regime. Faults distant from the injection well, in our simulations, experience lower injection-induced overpressure due to

pressure dissipation with distance; at these locations, capillary entry pressure becomes the primary determinant of whether leakage initiates at all. This spatial transition is directly evidenced in the correlation analysis: Fault 23 exhibits permeability sensitivity approximately an order of magnitude larger than its capillary entry pressure sensitivity, while farther faults such as Fault 14 and Faults 2-5 show relatively stronger capillary sensitivity despite weaker aggregate influence on total leakage. This spatial distinction also has a temporal dimension: faults in close proximity to the injection well are exposed to peak injection-induced overpressure during the 30-year injection period and are therefore likely to leak predominantly during operations, whilst faults distant from the well are reached only after CO_2 has migrated updip during the post-injection period, representing a longer-term post-injection risk horizon. A characterisation programme can be sequenced accordingly, prioritising permeability measurement for the updip fault subset where overpressure drive is sustained, while capillary entry pressure measurements constrain leakage onset thresholds for all faults. In practice, both would rely on analogue fault data from similar clastic settings where direct core measurements are unavailable (Faulkner et al., 2010; Bense et al., 2013; Busch & Amann-Hildenbrand, 2013; Espinoza & Santamarina, 2017).

The concentration of leakage along faults intercepting the updip migration pathway is consistent with field-scale studies showing that leakage outcomes concentrate in a small structural subset rather than distributing uniformly across fault populations (Gasda et al., 2022; Salo-Salgado et al., 2025). Only 5 of 23 faults exhibit significant correlation with total leakage, all positioned along the primary plume migration pathway, which suggests that structural geometry provides a practical first-order guide for focusing characterisation investment even before detailed fault property data are available. Fault 23 dominates system response consistent with its position at the primary updip migration pathway, and targeted characterisation of this fault alone would substantially reduce current predictive uncertainty relative to uniform sampling across the full fault population. The gateway behaviour of Fault 1 is a qualitatively different result that structural position cannot predict: its transmissibility controls lateral access to an entire northern fault array, such that low transmissibility isolates this domain regardless of the individual properties of faults downstream. This cascade pathway mechanism is invisible to single-fault sensitivity analysis, which would assign negligible influence on Fault 1 based on its permeability correlation alone, and demonstrates that multi-fault uncertainty quantification is necessary to resolve system-level leakage behaviour in structurally complex settings. Recent approaches have advanced fault leakage uncertainty quantification, applying full two-phase physics and geomechanical coupling to single-fault systems (Lu et al., 2025) or copula representation of dependent fault properties within a single fault zone (Pettersson et al., 2025); the present study complements these by resolving the cascade interactions that emerge across a 23-fault population simultaneously. The conditional cluster probability analysis translates this ranking into concrete characterisation targets, identifying the specific parameter values at which leakage regime membership shifts and providing actionable measurement thresholds that the Spearman ranking alone cannot supply.

The 44% modal frequency of high-leakage realisations reflects the breadth of current parameter uncertainty rather than an inherent property of the storage site. As fault properties are constrained through targeted characterisation, parameter uncertainty narrows and realisations shift toward the cluster consistent with measured values; this

may confirm lower leakage risk or reveal that high-leakage conditions are more probable than current parameter distributions suggest (Alcalde et al., 2018). The three medoid scenarios are specific, physically realisable parameter combinations that can be used directly as inputs to detailed 3D coupled simulations, enabling assessment of effects excluded here without evaluating the full ensemble (Scheidt & Caers, 2009; Mahjour & Faroughi, 2023).

CO_2 movement to the overlying aquifer via fault damage zones is classified as leakage in this analysis, as it exits the defined storage formation into a separate compartment. Under typical regulatory frameworks, such flux would instead be classified as migration if the overlying aquifer were formally designated within the storage complex boundary (Dixon et al., 2015; Krevor et al., 2023). The distinction carries regulatory weight: leakage implies loss of containment assurance, whereas within-complex migration implies redistribution within a characterised volume. For early-stage screening, the conservative interpretation is appropriate; storage complex boundary definitions would be established as part of the permitting process for any project advancing toward the permitting stage.

The analysis treats fault properties as uniform within each fault but heterogeneous across the 23-fault population, and as temporally constant throughout the simulation period. Real fault zones exhibit spatial variability along strike and depth, with preferential leakage pathways developing through clay-smear discontinuities and damage-zone variability (Berge et al., 2022; Snippe et al., 2022; Salo-Salgado et al., 2023; Rizzo et al., 2024). Within-fault heterogeneity was excluded to maintain tractability across 10,000 realisations; the independent sampling of properties across 23 faults partially addresses between-fault variability but does not capture co-variation between structurally related faults that copula-based approaches can resolve (Pettersson et al., 2025). The model neglects geomechanical coupling and non-isothermal transport effects, assuming instead that CO_2 has equilibrated thermally with formation temperature prior to reaching the fault zone. Geomechanical effects could modify leakage through stress-induced permeability changes and fault reactivation (Rutqvist, 2012; Ellsworth, 2013; Rinaldi et al., 2014; Vilarrasa et al., 2019; Zhao and Jha, 2019; Chen et al., 2024; Zheng et al., 2025). Recent probabilistic fault stability assessment emphasise the importance of fault throw relative to reservoir thickness and pore pressure change in evaluating reactivation risks (Yoon et al., 2023; Bisdom & Chan, 2024), and integrated mechanical and dynamic fault analyses would complement the present screening approach for sites where geomechanical risk is elevated. Reservoir property uncertainty influences CO_2 migration rates and plume geometry, and therefore which faults are contacted and when; this is captured partially through the reservoir exponent distributions but not through spatially variable porosity and permeability fields. The k-medoids clustering includes total fault leakage as a weighted variable in the distance metric, orienting cluster boundaries toward leakage behaviour rather than pure parameter-space proximity; while the qualitative three-regime separation is expected to be robust to moderate changes in this choice, the precise cluster boundaries and medoid positions are conditioned on the weighting applied, and systematic testing of alternative schemes remains a direction for methodological refinement.

The computational efficiency of the approach, with each simulation completing in under 30 seconds, is what makes the 10,000 realisations tractable as an early-stage screening tool rather than a dedicated research exercise. This efficiency is particularly consequential in settings such as the Malay Basin, where Malaysia's CCS deployment

targets require systematic evaluation of fault leakage risk across multiple aquifer intervals and structural configurations within compressed timescales (Fernandez et al., 2024; de Jonge-Anderson et al., 2025a). The workflow demonstrated here, combining rapid fault leakage screening with ensemble uncertainty quantification, Spearman sensitivity analysis, k-medoids clustering, and conditional cluster probability analysis, provides a transferable framework for early-stage risk characterisation in any faulted storage setting where comprehensive fault property data are unavailable at the time of site screening.

6 Conclusions

This study demonstrates rapid risk assessment for CO_2 storage in structurally complex basins. Application to the 23-fault system in the Malay Basin's Group J aquifer shows that computationally efficient screening tools enable systematic evaluation of well locations and fault property uncertainties. Evaluation of 600 well locations using sequential filtering on overpressure, boundary connectivity, and CO_2 retention identified an optimal injection site in the southwestern structural depression, where fault-bounded compartmentalisation limits lateral boundary losses while maintaining adequate transmissivity for pressure dissipation. Uncertainty quantification across 71 parameters using 10,000 Monte Carlo realisations reveals three key findings. First, leakage sensitivity concentrates spatially: only 5 of 23 faults exhibit significant correlation with outcomes, indicating that targeted characterisation of the updip fault subset would substantially reduce predictive uncertainty, rather than requiring comprehensive characterisation across the full fault population. Second, high-leakage scenarios comprise 44% of realisations under current parameter uncertainty, representing the modal outcome rather than a tail event, and reflecting that the current parameter distributions are insufficiently constrained to distinguish favourable from unfavourable outcomes. Third, cluster membership is predominantly controlled by Fault 23 permeability, exhibiting ~100-fold contrast between regimes, while Fault 1 transmissibility controls access to an entire downstream fault array, a cascade pathway that structural position alone cannot predict and single-fault analysis would miss. Conditional cluster probability analysis translates this ranking into concrete characterisation targets, identifying the specific parameter values at which leakage regime membership shifts, information the correlation ranking alone cannot supply. Together, these findings shift risk assessment from parameter sensitivity analysis to scenario identification, enabling site selection that balances operational targets against geological constraints. The computational efficiency, with each simulation completing in under 30 seconds, enables comprehensive uncertainty quantification supporting targeted data acquisition during early-stage screening.

Data Availability Statement

Simulations were conducted using co2-lab module of the open-source MATLAB Reservoir Simulation Toolbox (MRST), available at https://www.sintef.no/projectweb/mrst/. The fault leakage function module is on GitHub (https://github.com/Poriyalar/faultve) and available at Zenodo (https://doi.org/10.5281/zenodo.17469206). The Group J grid and an example script for loading it and mapping faults are available at Zenodo (https://doi.org/10.5281/zenodo.21137719).

Acknowledgements

The funding and data underpinning this work was provided by PETRONAS via the PETRONAS Centre of Excellence in Subsurface Engineering and Energy Transition (PACESET), based at Heriot-Watt University. Sebastian Geiger thanks Energi Simulation for supporting his Chair in Sustainable Geoenergy.

AI statement

During the preparation of this work the author(s) used Claude in order to improve the readability. After using this tool/service, the author(s) reviewed and edited the content as needed and take(s) full responsibility for the content of the published article.

CRediT Statement

Hariharan Ramachandran: Conceptualization, Methodology, Software, Validation, Formal analysis, Investigation, Writing - Original Draft, Visualization **Iain de-Jonge Anderson:** Formal analysis, Investigation, Resources, Data curation, Visualization, Writing - Review & Editing **Ana Widyanita:** Formal Analysis, Resources, Writing - Review & Editing **Uisdean Nicholson:** Formal analysis, Investigation, Resources, Data curation, Writing - Review & Editing, Supervision, Project administration, Funding acquisition **Andreas Busch:** Formal analysis, Investigation, Resources, Data curation, Writing - Review & Editing, Supervision, Project administration, Funding acquisition **Sebastian Geiger:** Conceptualization, Methodology, Investigation, Writing - Review & Editing, Supervision, Funding acquisition **Florian Doster:** Conceptualization, Methodology, Validation, Formal analysis, Investigation, Writing - Review & Editing, Supervision, Project administration, Funding acquisition

References

Alcalde, J., Flude, S., Wilkinson, M., Johnson, G., Edlmann, K., Bond, C. E., Scott, V., Gilfillan, S. M. V., Ogaya, X., & Haszeldine, R. S. (2018). Estimating geological CO2 storage security to deliver on climate mitigation. *Nature Communications*, *9*(1), 2201. https://doi.org/10.1038/s41467-018-04423-1

Andersen, O. (2017). Simplified models for numerical simulation of geological CO2 storage [Doctoral thesis, The University of Bergen]. https://bora.uib.no/bora-xmlui/handle/1956/15477

Andersen, O. A., Nilsen, H. M., & Gasda, S. E. (2016, August 29). *Modelling geomechanical impact of co2 injection and migration using precomputed response functions*. ECMOR XV - 15th European Conference on the Mathematics of Oil Recovery, Amsterdam, Netherlands. https://doi.org/10.3997/2214-4609.201601760

Andersen, O., Gasda, S. E., & Nilsen, H. M. (2015). Vertically averaged equations with variable density for co2 flow in porous media. *Transport in Porous Media*, *107*(1), 95–127. https://doi.org/10.1007/s11242-014-0427-z

Ashworth, P., Wade, S., Reiner, D., & Liang, X. (2015). Developments in public communications on CCS. *International Journal of Greenhouse Gas Control*, *40*, 449–458. https://doi.org/10.1016/j.ijggc.2015.06.002

Awad, M. M., & Espinoza, D. N. (2024). Mudrock wettability at pressure and temperature conditions for CO2 geological storage. *International Journal of Greenhouse Gas Control*, *135*, 104160. https://doi.org/10.1016/j.ijggc.2024.104160

Bandilla, K. W., Celia, M. A., & Leister, E. (2014). Impact of model complexity on co2 plume modeling at sleipner. *Energy Procedia*, *63*, 3405–3415. https://doi.org/10.1016/j.egypro.2014.11.369

Bense, V. F., & Person, M. A. (2006). Faults as conduit-barrier systems to fluid flow in siliciclastic sedimentary aquifers. *Water Resources Research*, *42*(5), 2005WR004480. https://doi.org/10.1029/2005WR004480

Bense, V. F., Gleeson, T., Loveless, S. E., Bour, O., & Scibek, J. (2013). Fault zone hydrogeology. *Earth-Science Reviews*, *127*, 171–192. https://doi.org/10.1016/j.earscirev.2013.09.008

Berge, R. L., Gasda, S. E., Keilegavlen, E., & Sandve, T. H. (2022). Impact of deformation bands on fault-related fluid flow in field-scale simulations. *International Journal of Greenhouse Gas Control*, *119*, 103729. https://doi.org/10.1016/j.ijggc.2022.103729

Bielicki, J. M., Peters, C. A., Fitts, J. P., & Wilson, E. J. (2015). An examination of geologic carbon sequestration policies in the context of leakage potential. *International Journal of Greenhouse Gas Control*, *37*, 61–75. https://doi.org/10.1016/j.ijggc.2015.02.023

Birkholzer, J. T., & Zhou, Q. (2009). Basin-scale hydrogeologic impacts of CO2 storage: Capacity and regulatory implications. *International Journal of Greenhouse Gas Control*, *3*(6), 745–756. https://doi.org/10.1016/j.ijggc.2009.07.002

Birkholzer, J. T., Cihan, A., & Zhou, Q. (2012). Impact-driven pressure management via targeted brine extraction—Conceptual studies of CO2 storage in saline formations. *International Journal of Greenhouse Gas Control*, *7*, 168–180. https://doi.org/10.1016/j.ijggc.2012.01.001

Bisdom, K., & Chan, A. W. (2024). De-risking fault leakage risk and containment integrity for subsurface storage applications. *iScience*, *27*(6), 109957. https://doi.org/10.1016/j.isci.2024.109957

Bjørnarå, T. I., Nordbotten, J. M., & Park, J. (2016). Vertically integrated models for coupled two-phase flow and geomechanics in porous media. *Water Resources Research*, *52*(2), 1398–1417. https://doi.org/10.1002/2015WR017290

Bump, A. P., & Hovorka, S. D. (2024). Pressure space: The key subsurface commodity for CCS. *International Journal of Greenhouse Gas Control*, *136*, 104174. https://doi.org/10.1016/j.ijggc.2024.104174

Busch, A., & Amann-Hildenbrand, A. (2013). Predicting capillarity of mudrocks. *Marine and Petroleum Geology*, *45*, 208–223. https://doi.org/10.1016/j.marpetgeo.2013.05.005

Busch, A., & Kampman, N. (2018). Migration and leakage of co_2 from deep geological storage sites. In S. Vialle, J. Ajo-Franklin, & J. W. Carey (Eds.), *Geophysical Monograph Series* (1st ed., pp. 283–303). Wiley. https://doi.org/10.1002/9781119118657.ch14

Caine, J. S., Evans, J. P., & Forster, C. B. (1996). Fault zone architecture and permeability structure. *Geology*, *24*(11), 1025. https://doi.org/10.1130/0091-7613(1996)024<1025:FZAAPS>2.3.CO;2

Chen, L., Elsworth, D., Chen, J., & Gan, Q. (2024). Evaluation of CO2 leakage potential through fault instability in CO2 geological sequestration by coupled THMC modelling. *Gas Science and Engineering*, *132*, 205486. https://doi.org/10.1016/j.jgsce.2024.205486

Childs, C., Manzocchi, T., Walsh, J. J., Bonson, C. G., Nicol, A., & Schöpfer, M. P. J. (2009). A geometric model of fault zone and fault rock thickness variations. *Journal of Structural Geology*, *31*(2), 117–127. https://doi.org/10.1016/j.jsg.2008.08.009

Cihan, A., Birkholzer, J. T., & Bianchi, M. (2015). Optimal well placement and brine extraction for pressure management during CO2 sequestration. *International Journal of Greenhouse Gas Control*, *42*, 175–187. https://doi.org/10.1016/j.ijggc.2015.07.025

Cihan, A., Guglielmi, Y., Glubokovskikh, S., Cao, M., Rutqvist, J., Jordan, P., Reagan, M., & Birkholzer, J. (2026). A boundary element model for assessing large-scale pressurization in faulted geological storage systems. *Water Resources Research*, *62*(3), e2025WR041198. https://doi.org/10.1029/2025WR041198

de Jonge-Anderson, I. (2025b). *Iaindejongeanderson/malaybasin_co2_storage: Supplementary data for article "regional screening of saline aquifers in the malay basin for co2 storage"* [Computer software]. Zenodo. https://doi.org/10.5281/ZENODO.14761426

De Jonge-Anderson, I., Johnson, G., Alcalde, J., & Roberts, J. J. (2026). *CO2LOGIX: A first-order model of pressure-constrained CO2 geological storage growth at the basin scale*. https://doi.org/10.2139/ssrn.5711833

de Jonge-Anderson, I., Ramachandran, H., Nicholson, U., Geiger, S., Widyanita, A., & Doster, F. (2024a). Determining CO2 storage efficiency within a saline aquifer using reduced complexity models. Advances in Geo-Energy Research, 13(1), 22–31. https://doi.org/10.46690/ager.2024.07.04

de Jonge-Anderson, I., Ramachandran, H., Widyanita, A., Busch, A., Doster, F., & Nicholson, U. (2025a). Regional screening of saline aquifers in the Malay Basin for CO2 storage. *International Journal of Greenhouse Gas Control*, *143*, 104347. https://doi.org/10.1016/j.ijggc.2025.104347

de Jonge-Anderson, I., Widyanita, A., Busch, A., Doster, F., & Nicholson, U. (2024b). New insights into the structural and stratigraphic evolution of the Malay Basin using 3D seismic data: Implications for regional carbon capture and storage potential. Basin Research, 36(4), e12885. https://doi.org/10.1111/bre.12885

Department of Geology, Universiti Malaya, 50603 Kuala Lumpur, Malaysia, & Madon, M. (2021). Five decades of petroleum exploration and discovery in the malay basin (1968-2018) and remaining potential. *Bulletin Of The Geological Society Of Malaysia*, *72*, 63–88. https://doi.org/10.7186/bgsm72202106

Dixon, T., McCoy, S. T., & Havercroft, I. (2015). Legal and regulatory developments on ccs. *International Journal of Greenhouse Gas Control*, *40*, 431–448. https://doi.org/10.1016/j.ijggc.2015.05.024

Doster, F., Nordbotten, J. M., & Celia, M. A. (2013). Impact of capillary hysteresis and trapping on vertically integrated models for CO2 storage. *Advances in Water Resources*, *62*, 465–474. https://doi.org/10.1016/j.advwatres.2013.09.005

Ellsworth, W. L. (2013). Injection-induced earthquakes. *Science*, *341*(6142), 1225942. https://doi.org/10.1126/science.1225942

Espinoza, D. N., & Santamarina, J. C. (2017). CO2 breakthrough—Caprock sealing efficiency and integrity for carbon geological storage. International Journal of Greenhouse Gas Control, 66, 218–229. https://doi.org/10.1016/j.ijggc.2017.09.019

Faulkner, D. R., Jackson, C. A. L., Lunn, R. J., Schlische, R. W., Shipton, Z. K., Wibberley, C. A. J., & Withjack, M. O. (2010). A review of recent developments concerning the structure, mechanics and fluid flow properties of fault zones. *Journal of Structural Geology*, *32*(11), 1557–1575. https://doi.org/10.1016/j.jsg.2010.06.009

Faulkner, D. R., Mitchell, T. M., Jensen, E., & Cembrano, J. (2011). Scaling of fault damage zones with displacement and the implications for fault growth processes. *Journal of Geophysical Research*, *116*(B5), B05403. https://doi.org/10.1029/2010JB007788

Fernandez, M. I., Go, Y. I., Wong, M. L. D., & Früh, W.-G. (2024). Malaysia's energy transition and readiness towards attaining net zero: Review of the potential, constraints, and enablers. *Renewable Energy Focus*, *51*, 100640. https://doi.org/10.1016/j.ref.2024.100640

Freites, A., Corbett, P., Rongier, G., & Geiger, S. (2023). Automated classification of well test responses in naturally fractured reservoirs using unsupervised machine learning. *Transport in Porous Media*, *147*(3), 747–779. https://doi.org/10.1007/s11242-023-01929-1

Gasda, S., Keilegavlen, E., Sandve, T. H., Berge, R., Pettersson, P., & Krumscheid, S. (2022). Practical field-scale simulation approaches for quantification of fault-related leakage under uncertainty. *SSRN Electronic Journal*. https://doi.org/10.2139/ssrn.4277020

González-Nicolás, A., Cihan, A., Petrusak, R., Zhou, Q., Trautz, R., Riestenberg, D., Godec, M., & Birkholzer, J. T. (2019). Pressure management via brine extraction in geological CO2 storage: Adaptive optimization strategies under poorly characterized reservoir conditions.

International Journal of Greenhouse Gas Control, *83*, 176–185. https://doi.org/10.1016/j.ijggc.2019.02.009

Guiltinan, E. J., Espinoza, D. N., Cockrell, L. P., & Cardenas, M. B. (2018). Textural and compositional controls on mudrock breakthrough pressure and permeability. *Advances in Water Resources*, *121*, 162–172. https://doi.org/10.1016/j.advwatres.2018.08.014

Hasbollah, D. Z. A., Junin, R., Taib, A. M., & Mazlan, A. N. (2020). Basin evaluation of co2 geological storage potential in malay basin, malaysia. In P. Duc Long & N. T. Dung (Eds.), Geotechnics for Sustainable Infrastructure Development (Vol. 62, pp. 1405–1410). Springer Singapore. https://doi.org/10.1007/978-981-15-2184-3_184

Huppert, H. E., & Woods, A. W. (1995). Gravity-driven flows in porous layers. *Journal of Fluid Mechanics*, *292*, 55–69. https://doi.org/10.1017/S0022112095001431

Jha, B., & Juanes, R. (2014). Coupled multiphase flow and poromechanics: A computational model of pore pressure effects on fault slip and earthquake triggering. *Water Resources Research*, *50*(5), 3776–3808. https://doi.org/10.1002/2013WR015175

Jones, C. R., Olfe-Kräutlein, B., Naims, H., & Armstrong, K. (2017). The social acceptance of carbon dioxide utilisation: A review and research agenda. *Frontiers in Energy Research*, *5*, 11. https://doi.org/10.3389/fenrg.2017.00011

Kang, M., Nordbotten, J. M., Doster, F., & Celia, M. A. (2014). Analytical solutions for two-phase subsurface flow to a leaky fault considering vertical flow effects and fault properties. Water Resources Research, 50(4), 3536–3552. https://doi.org/10.1002/2013WR014628

Krevor, S., De Coninck, H., Gasda, S. E., Ghaleigh, N. S., De Gooyert, V., Hajibeygi, H., Juanes, R., Neufeld, J., Roberts, J. J., & Swennenhuis, F. (2023). Subsurface carbon dioxide and hydrogen storage for a sustainable energy future. Nature Reviews Earth & Environment, 4(2), 102–118. https://doi.org/10.1038/s43017-022-00376-8

Lie, K.-A. (2019). An introduction to reservoir simulation using matlab/gnu octave: User guide for the matlab reservoir simulation toolbox(Mrst) (1st ed.). Cambridge University Press. https://doi.org/10.1017/9781108591416

Lu, H., Saló-Salgado, L., Marzouk, Y. M., & Juanes, R. (2025). Uncertainty quantification of fluid leakage and fault instability in geologic co2 storage. *Water Resources Research*, *61*(10), e2024WR039275. https://doi.org/10.1029/2024WR039275

Madon, M., Yang, J.-S., Abolins, P., Hassan, R. A., Yakzan, A. M., & Zainal, S. B. (2004). *Petroleum systems of the northern malay basin*. https://archives.datapages.com/data/geological-society-of-malaysia/bulletins/049/049001/pdfs/125.htm

Mahjour, S. K., & Faroughi, S. A. (2023). Selecting representative geological realizations to model subsurface CO 2 storage under uncertainty. *International Journal of Greenhouse Gas Control*, *127*, 103920. https://doi.org/10.1016/j.ijggc.2023.103920

Malaysian Continental Shelf Project, National Security Council, Malaysia, Madon, M., Jong, J., & JX Nippon Oil and Gas Exploration (Malaysia) Limited, Malaysia. (2021). Geothermal gradient and heat flow maps of offshore malaysia: Some updates and observations. Bulletin of the Geological Society of Malaysia, 71, 159–183. https://doi.org/10.7186/bgsm71202114

Manzocchi, T., Childs, C., & Walsh, J. J. (2010). Faults and fault properties in hydrocarbon flow models. Geofluids, 10(1–2), 94–113. https://doi.org/10.1111/j.1468-8123.2010.00283.x

McKay, M. D., Beckman, R. J., & Conover, W. J. (1979). A comparison of three methods for selecting values of input variables in the analysis of output from a computer code. *Technometrics*, *21*(2), 239. https://doi.org/10.2307/1268522

Mears, E. M., Underhill, J. R., & De Jonge-Anderson, I. (2026). The role of structural compartmentalization in carbon storage site selection in Permian (Rotliegend group) reservoirs in the Southern North Sea. *Energy Geoscience Conference Series*, *1*(1), egc1-2023–2036. https://doi.org/10.1144/egc1-2023-36

Meguerdijian, S., & Jha, B. (2021). Quantification of fault leakage dynamics based on leakage magnitude and dip angle. *International Journal for Numerical and Analytical Methods in Geomechanics*, *45*(16), 2303–2320. https://doi.org/10.1002/nag.3267

Mhlambi, S., Eruteya, O. E., Agbor, F. A., Moscariello, A., Van Bever Donker, J. M., & Samankassou, E. (2025). Assessing CO2 storage potential in a structurally complex depleted gas reservoir, offshore South Africa. *Carbon Capture Science & Technology*, *17*, 100499. https://doi.org/10.1016/j.ccst.2025.100499

Miocic, J. M., Gilfillan, S. M. V., Frank, N., Schroeder-Ritzrau, A., Burnside, N. M., & Haszeldine, R. S. (2019a). 420,000 year assessment of fault leakage rates shows geological carbon storage is secure. *Scientific Reports*, *9*(1), 769. https://doi.org/10.1038/s41598-018-36974-0

Miocic, J. M., Johnson, G., & Bond, C. E. (2019b). Uncertainty in fault seal parameters: Implications for CO_2 column height retention and storage capacity in geological CO_2 storage projects. *Solid Earth*, *10*(3), 951–967. https://doi.org/10.5194/se-10-951-2019

Møyner, O., & Nilsen, H. M. (2019). Multiresolution coupled vertical equilibrium model for fast flexible simulation of CO2 storage. *Computational Geosciences*, *23*(1), 1–20. https://doi.org/10.1007/s10596-018-9775-z

Neufeld, J. A., Vella, D., & Huppert, H. E. (2009). The effect of a fissure on storage in a porous medium. Journal of Fluid Mechanics, 639, 239–259. https://doi.org/10.1017/S0022112009991030

Nilsen, H. M., Lie, K.-A., & Andersen, O. (2016). Fully-implicit simulation of vertical-equilibrium models with hysteresis and capillary fringe. *Computational Geosciences*, *20*(1), 49–67. https://doi.org/10.1007/s10596-015-9547-y

Nilsen, H. M., Lie, K.-A., & Andersen, O. (2016). Robust simulation of sharp-interface models for fast estimation of CO2 trapping capacity in large-scale aquifer systems. *Computational Geosciences*, *20*(1), 93–113. https://doi.org/10.1007/s10596-015-9549-9

Nilsen, H., Herrera, P. A., Ashraf, M., Ligaarden, I., Iding, M., Hermanrud, C., Lie, K.-A., Nordbotten, J. M., Dahle, H. K., & Keilegavlen, E. (2011). Field-case simulation of CO2 -plume migration using vertical-equilibrium models. *Energy Procedia*, *4*, 3801–3808. https://doi.org/10.1016/j.egypro.2011.02.315

Nilsen, H., Lie, K.-A., & Andersen, O. (2015). Analysis of CO2 trapping capacities and long-term migration for geological formations in the Norwegian North Sea using MRST-co2lab. *Computers & Geosciences*, *79*, 15–26. https://doi.org/10.1016/j.cageo.2015.03.001

Nordbotten, J. M., & Celia, M. A. (2011). Geological storage of co2: Modeling approaches for large-scale simulation (1st ed.). Wiley. https://doi.org/10.1002/9781118137086

Ougier-Simonin, A., Tucker, O., Bump, A., Gasda, S. E., Otterlei, R. E., Lemgruber-Traby, A., Mackay, E., Ricard, L. P., Herrmann, F., & Imhof, M. (2026). The pressure balancing act in geological storage: Sharing the subsurface for the common good. *International Journal of Greenhouse Gas Control*, *151*, 104610. https://doi.org/10.1016/j.ijggc.2026.104610

Park, H.-S., & Jun, C.-H. (2009). A simple and fast algorithm for K-medoids clustering. *Expert Systems with Applications*, *36*(2), 3336–3341. https://doi.org/10.1016/j.eswa.2008.01.039

PETRONAS. (2022). Geological & geophysical information of the Malay Basin. Malaysia Bid round 2022. https://www.petronas.com/sites/mpm/files/2022-07/MBR-2022-Regional-Overview-Peninsular-Malaysia.pdf (accessed June 2024).

Pettersson, P., Keilegavlen, E., Sandve, T. H., Gasda, S. E., & Krumscheid, S. (2025). Copula modeling and uncertainty propagation in field-scale simulation of CO_2 fault leakage. *Water Resources Research*, *61*(1), e2024WR038073. https://doi.org/10.1029/2024WR038073

Phillips, T., Kampman, N., Bisdom, K., Forbes Inskip, N. D., Den Hartog, S. A. M., Cnudde, V., & Busch, A. (2020). Controls on the intrinsic flow properties of mudrock fractures: A review of their importance in subsurface storage. *Earth-Science Reviews*, *211*, 103390. https://doi.org/10.1016/j.earscirev.2020.103390

Ramachandran, H., De Jonge-Anderson, I., Hafizi Musa, I., Nicholson, U., Tan, C. P., Geiger, S., & Doster, F. (2026). Rapid fault leakage modelling for co_2 storage in saline aquifers. *Water Resources Research*, *62*(4), e2025WR041074. https://doi.org/10.1029/2025WR041074

Rinaldi, A. P., Rutqvist, J., & Cappa, F. (2014). Geomechanical effects on CO2 leakage through fault zones during large-scale underground injection. *International Journal of Greenhouse Gas Control*, 20, 117–131. https://doi.org/10.1016/j.ijggc.2013.11.001

Ringrose, P. S., & Meckel, T. A. (2019). Maturing global CO2 storage resources on offshore continental margins to achieve 2DS emissions reductions. *Scientific Reports*, *9*(1), 17944. https://doi.org/10.1038/s41598-019-54363-z

Rizzo, R. E., Inskip, N. F., Fazeli, H., Betlem, P., Bisdom, K., Kampman, N., Snippe, J., Senger, K., Doster, F., & Busch, A. (2024). Modelling geological CO2 leakage: Integrating fracture permeability and fault zone outcrop analysis. *International Journal of Greenhouse Gas Control*, *133*, 104105. https://doi.org/10.1016/j.ijggc.2024.104105

Rutqvist, J. (2012). The geomechanics of co2 storage in deep sedimentary formations. *Geotechnical and Geological Engineering*, *30*(3), 525–551. https://doi.org/10.1007/s10706-011-9491-0

Saló-Salgado, L., Davis, S., & Juanes, R. (2023). Fault permeability from stochastic modeling of clay smears. *Geology*, *51*(1), 91–95. https://doi.org/10.1130/G50739.1

Saló-Salgado, L., Silva, J. A., Lun, L., Rogers, C. M., Davis, J. S., & Juanes, R. (2025). Assessing co2 migration within faults during megatonne-scale geologic carbon dioxide storage in offshore texas. *Water Resources Research*, *61*(5), e2024WR037059. https://doi.org/10.1029/2024WR037059

Saltelli, A., Ratto, M., Andres, T., Campolongo, F., Cariboni, J., Gatelli, D., Saisana, M., & Tarantola, S. (2007). *Global sensitivity analysis. The primer* (1st ed.). Wiley. https://doi.org/10.1002/9780470725184

Scheidt, C., & Caers, J. (2009). Representing spatial uncertainty using distances and kernels. *Mathematical Geosciences*, *41*(4), 397–419. https://doi.org/10.1007/s11004-008-9186-0

Scibek, J. (2020). Multidisciplinary database of permeability of fault zones and surrounding protolith rocks at world-wide sites. *Scientific Data*, *7*(1), 95. https://doi.org/10.1038/s41597-020-0435-5

Snippe, J., Kampman, N., Bisdom, K., Tambach, T., March, R., Maier, C., Phillips, T., Inskip, N. F., Doster, F., & Busch, A. (2022). Modelling of long-term along-fault flow of CO2 from a natural reservoir. International Journal of Greenhouse Gas Control, 118, 103666. https://doi.org/10.1016/j.ijggc.2022.103666

Torabi, A., & Berg, S. S. (2011). Scaling of fault attributes: A review. *Marine and Petroleum Geology*, *28*(8), 1444–1460. https://doi.org/10.1016/j.marpetgeo.2011.04.003

Vilarrasa, V., Carrera, J., Olivella, S., Rutqvist, J., & Laloui, L. (2019). Induced seismicity in geologic carbon storage. *Solid Earth*, *10*(3), 871–892. https://doi.org/10.5194/se-10-871-2019

Vilarrasa, V., Makhnenko, R. Y., & Laloui, L. (2017). Potential for fault reactivation due to co2 injection in a semi-closed saline aquifer. *Energy Procedia*, *114*, 3282–3290. https://doi.org/10.1016/j.egypro.2017.03.1460

Yoon, S., Lee, H., & Kim, J. (2023). The modeling of fault activation, slip, and induced seismicity for geological CO2 storage at a pilot-scale site in the Janggi Basin, South Korea. *International Journal of Rock Mechanics and Mining Sciences*, *170*, 105441. https://doi.org/10.1016/j.ijrmms.2023.105441

Yortsos, Y. C. (1995). A theoretical analysis of vertical flow equilibrium. Transport in Porous Media, 18(2), 107–129. https://doi.org/10.1007/BF01064674

Zhang, K., & Lau, H. C. (2022). Regional opportunities for CO2 capture and storage in Southeast Asia. *International Journal of Greenhouse Gas Control*, *116*, 103628. https://doi.org/10.1016/j.ijggc.2022.103628

Zhao, X., & Jha, B. (2019). Role of well operations and multiphase geomechanics in controlling fault stability during co_2 storage and enhanced oil recovery. *Journal of Geophysical Research: Solid Earth*, *124*(7), 6359–6375. https://doi.org/10.1029/2019JB017298

Zheng, F., Jha, B., & Jafarpour, B. (2025). Mitigating caprock failure and leakage risks through controlled CO2 injection and coupled flow-geomechanics-fracturing simulation. *International Journal of Greenhouse Gas Control*, *144*, 104387. https://doi.org/10.1016/j.ijggc.2025.104387

Zhou, Q., & Birkholzer, J. T. (2011). On scale and magnitude of pressure build-up induced by large-scale geologic storage of CO_2. *Greenhouse Gases: Science and Technology*, *1*(1), 11–20. https://doi.org/10.1002/ghg3.1

Zhou, Q., Birkholzer, J. T., Tsang, C.-F., & Rutqvist, J. (2008). A method for quick assessment of CO2 storage capacity in closed and semi-closed saline formations. *International Journal of Greenhouse Gas Control*, *2*(4), 626–639. https://doi.org/10.1016/j.ijggc.2008.02.004

842